

# Scaling, domains, and states in the four-dimensional random field Ising magnet

A. Alan Middleton

*Department of Physics, Syracuse University, Syracuse, New York 13244*

(Dated: August 8, 2002)

The four dimensional Gaussian random field Ising magnet is investigated numerically at zero temperature, using samples up to size  $64^4$ , to test scaling theories and to investigate the nature of domain walls and the thermodynamic limit. As the magnetization exponent  $\beta$  is more easily distinguishable from zero in four dimensions than in three dimensions, these results provide a useful test of conventional scaling theories. Results are presented for the critical behavior of the heat capacity, magnetization, and stiffness. The fractal dimensions of the domain walls at criticality are estimated. A notable difference from three dimensions is the structure of the spin domains: frozen spins of both signs percolate at a disorder magnitude less than the value at the ferromagnetic to paramagnetic transition. Hence, in the vicinity of the transition, there are two percolating clusters of opposite spins that are fixed under any boundary conditions. This structure changes the interpretation of the domain walls for the four dimensional case. The scaling of the effect of boundary conditions on the interior spin configuration is found to be consistent with the domain wall dimension. There is no evidence of a glassy phase: there appears to be a single transition from two ferromagnetic states to a single paramagnetic state, as in three dimensions. The slowing down of the ground state algorithm is also used to study this model and the links between combinatorial optimization and critical behavior.

## I. INTRODUCTION

As the random field Ising magnet (RFIM) is a relatively well-studied model of a disordered material, general questions about thermodynamic phases and transitions have been addressed using it as a model system. Experimental studies of random field Ising magnets are also available for comparison with theoretical predictions. The statics of the RFIM have been studied in detail theoretically, both analytically and numerically. It has been proven that there are at least two phases in dimensions greater than two,<sup>1</sup> scaling arguments have been constructed,<sup>2</sup> the replica approach has been applied,<sup>3</sup> and the model has been analyzed on hierarchical lattices.<sup>4</sup> The RFIM also has a rich numerical history, including extensive Monte Carlo simulations<sup>5-8</sup> and zero temperature ground state studies.<sup>9-17</sup> Some questions about the model remain unsettled, though, and the physical picture of excitations is somewhat incomplete. Studying these properties of the model will be useful in building a more complete picture, especially when addressing questions about dynamics.

There has been an active discussion about the nature of the phase diagram for the random field Ising model (RFIM). One controversy has been whether the transition from the ferromagnetic phase to paramagnetic phase, which occurs as the disorder strength or temperature is varied, is continuous in three dimensions.<sup>2,5,12,13</sup> Recent work<sup>16,17</sup> provides further strong evidence that the transition is second order in this case and that previously derived scaling relations apply. However, as the ratio  $\beta/\nu$  of the order parameter exponent  $\beta$  to the correlation length exponent  $\nu$  is very small, some scaling predictions are hard to verify. It is of interest to pursue this investigation in higher dimension, where  $\beta/\nu$  is larger, to verify the general theoretical picture suggested

for the RFIM in finite dimensions.

## II. SUMMARY OF RESULTS

Numerical simulations have been carried out for the Gaussian RFIM on a simple hypercubic lattice in four dimensions. The Hamiltonian (for a review of the RFIM see Ref. 2) is defined over spin configurations  $\{s_i = \pm 1\}$ ,

$$H = -J \sum_{\langle ij \rangle} s_i s_j - \sum_i h_i s_i, \quad (1)$$

with  $\langle ij \rangle$  indicating nearest neighbor sites  $i, j$  and the random fields  $h_i$  are chosen independently from a Gaussian distribution with mean zero and variance  $h^2$ . Here the energy scale is fixed by setting  $J = 1$  in the computations, with temperature  $T = 0$ . Exact ground states for this Hamiltonian are found using a max-flow algorithm, as in previous work.<sup>9-17</sup>

The magnetization is more useful in studying the 4D RFIM than the 3D RFIM, as the magnetization exponent  $\beta$  is more easily distinguished from zero. The Binder parameter is used to locate the ferromagnetic-to-paramagnetic transition relatively precisely at  $h_c = 4.179(2)$ . A finite-size study of the magnetization allows the ratio  $\beta/\nu$  to be estimated as  $\beta/\nu = 0.19(3)$ . Besides its relevance to the magnetization, this ratio is important in studying the nature of the states and comparing domain wall exponents.

The ground state energies and their dependence on boundary conditions can be used to study the heat capacity and stiffness exponents of the RFIM. The stiffness (violation of hyperscaling) exponent is determined to be  $\theta = 1.82 \pm 0.07$ , consistent with conventional exponent bounds.<sup>18,20</sup> Unlike the 3D case, the value for  $\theta$  is numerically distinguishable from  $d/2$ . The heat capacity

exponent inferred from the ground state energies is estimated as  $\alpha = 0.26 \pm 0.05$ , apparently distinct from  $\alpha = 0$  and again consistent with the conventional disorder variant of Widom scaling,<sup>18,19</sup>  $(d - \theta)\nu = 2 - \alpha$ .

The spatial structure of the spins for the 4D RFIM is found to differ from the structure for the 3D RFIM, over the length scales studied. In the case of three dimensions, the spins appear to form a nested sets of domain walls at criticality.<sup>16,19</sup> In 4D, the frozen spins (those invariant under all boundary conditions) percolate in the ferromagnetic phase. This implies that domain walls cannot be simply identified as surfaces between connected sets of same-sign spins. Simulations show that the frozen spins percolate at a value  $h_p^f = 3.680(5)$ . At a slightly higher value of  $h$ ,  $h_p^m$ , the minority spins (frozen spins of a sign opposite to the magnetization) percolate. Evidence is given in Sec. VI that this percolation takes place even when the spins are coarse grained, with the critical value of  $h$  dependent on the scale of the coarse graining. While this percolation does *not* affect thermodynamic quantities such as the bond part of the mean ground state energy,  $\overline{E}_J$ , or the magnetization, the definition of the domain walls and the description of the spin-spin correlation function turns out to not be as straightforward as in the case of  $d = 3$ .

The qualitative nature of the thermodynamic limit in the 4D RFIM can be addressed by studying the influence of boundary conditions on the configuration in a fixed window. In Sec. VII, the effect of up (+) and down (-) boundary conditions at the surface of the sample are compared with periodic boundary conditions ( $P$ ). The probability of the interior spins in the  $P$  configuration being identical to either the + or - configuration approaches 1, as  $L \rightarrow \infty$ , for all  $h$ . Taking the periodic boundary condition as a generic case, then, in the large volume limit, the interior of the ground state configuration is found in one of the two ferromagnetic states for  $h < h_c$  or the paramagnetic state for  $h > h_c$ . The probability for the  $P$  configuration to be either + or - in the interior scales in a manner consistent with the 3D results<sup>16</sup> and the general case where there are few states in the thermodynamic limit.<sup>21</sup>

### A. Algorithm and error bars

The variant of the push-relabel algorithm used is the same as described in Ref. 16. Near criticality, ground states for samples of size  $64^4$  were found in about 3000 s using 1 GHz Pentium III processors. Ground states for smaller samples were found using a faster, but less memory-efficient, version of the algorithm; using the same processors, near-critical samples of volume  $32^4$  were solved in approximately 60 s.

Error bars for exponent values throughout this paper include both estimated systematic errors due to apparent finite size effects and errors due to statistical uncertainties; the error bars represent an estimated range of

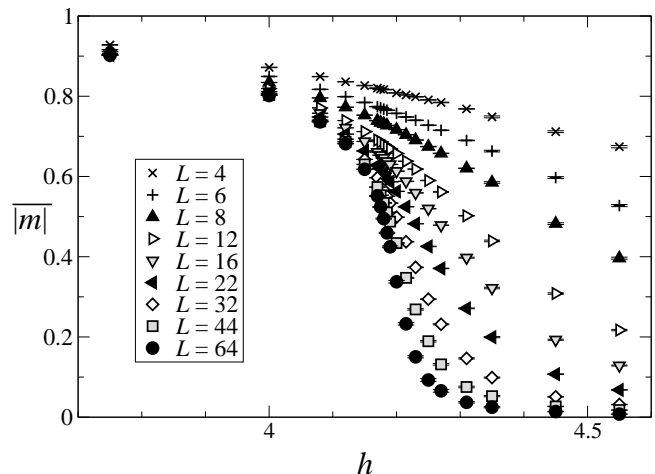


FIG. 1: Plot of the sample average of the absolute value of the magnetization,  $\overline{|m|}$ , of the 4D RFIM as a function of disorder  $h$  and system size  $L$ , for periodic boundary conditions.

values in which the value lies, with high confidence. In contrast, error bars in the figures for raw data reflect  $1\sigma$  statistical uncertainties computed from the standard deviation, except for the Binder cumulant, where the error bars were computed by resampling. Plots of fitted values, such as estimated peak heights, include both statistical errors and an error bar that reflects fluctuations in values that result from varying the degree of the polynomial fit and the chosen range of the fit.

In some of the plots, exponent values that differ from the “best” value from other plots are used to scale the data, to indicate that there is some flexibility in the exponent values, depending on the method. All of the values derived for the exponents from various methods are consistent with each other to within statistical and estimated systematic errors. Table I gives a summary of the numerical values of the best estimates for the exponents.

## III. MAGNETIZATION

As the exponent  $\beta$  is more readily determined in the 4D RFIM, compared with the 3D case, it is useful in 4D to study the magnetization as a first guide to the critical behavior and to locate the transition. The mean value of the absolute value of the magnetization is defined as

$$\overline{|m|} = N^{-1} \overline{\left| \sum_i s_i \right|}, \quad (2)$$

where the overline indicates an average over samples of volume  $N = L^4$ . The magnetization is directly computed for each sample from the ground state with periodic boundary conditions. The dependence of the sample-averaged magnetization on disorder  $h$  is plotted in Fig. 1.

TABLE I: Table of numerical estimates for the 4D Gaussian RFIM on the simple hypercubic lattice.

Symbol	Value	Definition and data used
$h_c$	$4.179 \pm 0.002$	Critical value of the random field for coupling $J = 1$ . The critical point is determined primarily from scaling of magnetization distribution (e.g., Binder cumulant as shown in Fig. 2); this $h_c$ is consistent with extrapolation in $L$ of the location of peaks in the specific heat and the number of operations used to find the ground state and the value at which the probability of stiffness being zero is independent of $L$ .
$h_p^f$	$3.680 \pm 0.005$	Value of the random field at which the frozen spins percolate. Sec. VI.
$h_p^m$	$3.875 \pm 0.005$	Value of the random field at which the minority spins percolate. See Sec. VI and Fig. 11.
$\beta/\nu$	$0.19 \pm 0.03$	Ratio of magnetization exponent $\beta$ to correlation length exponent $\nu$ . Determined from the scaling of $ m $ vs. $L$ at criticality for $12 \leq L \leq 64$ . See Fig. 3, Fig. 4 and Sec. III.
$\alpha/\nu$	$0.31 \pm 0.04$	Heat capacity exponent $\alpha$ divided by $\nu$ . Found from peaks $C_{\max}(L)$ , computed from the derivative of fit to $\overline{E}_J(h, L)$ . See Figs. 6 and 7.
$(\alpha - 1)/\nu$	$-0.94 \pm 0.06$	Combination of heat capacity exponent $\alpha$ and $\nu$ . Found from fit to power law for the discrete estimate of $d\overline{E}_J/d\ln(L)$ evaluated at peak of $C$ .
$\nu$	$0.82 \pm 0.06$	Correlation length exponent. Jointly estimated from magnetization scaling, $\alpha/\nu$ and $(\alpha - 1)/\nu$ , and the scaling of the stiffness with $L$ . Consistent with the scaling of the width of the number of algorithm operations.
$\beta$	$0.16 \pm 0.03$	Magnetization exponent, found from $\beta/\nu$ and $\nu$ .
$\alpha$	$0.26 \pm 0.05$	Heat capacity exponent, found from $\alpha/\nu$ and $\nu$ .
$\theta$	$1.82 \pm 0.07$	Violation of hyperscaling or the scaling of the stiffness at $h_c$ . Found from scaling of stiffness with $L$ and $h - h_c$ , see Sec. V and Fig. 9.
$d_s$	$3.94 \pm 0.06$	Fractal dimension of connected domain wall at $h = h_c$ . Note that the result is indistinguishable from $d = 4$ . See Fig. 10 and Sec. V.
$d_I$	$3.20 \pm 0.12$	Incongruent fractal dimension of domain wall at criticality. Box counting of incongruent volumes (disconnected wall). See Sec. V. Consistent with scaling of state overlap probabilities shown in Fig. 13 and Fig. 14.
$d_J$	$2.94 \pm 0.12$	Energy “fractal dimension” at $h = h_c$ . Found from the exchange part, $\Sigma_J$ , of the stiffness. See Fig. 10 and Sec. V.

### A. Binder cumulant and $h_c$

One method for determining the value of  $h_c$  is to use the Binder cumulant. The value of the cumulant,  $g = (3 - \overline{m^4}/\overline{m^2}^2)/2$ , should be  $g = 1$  in the ferromagnetic phase and should take on the value  $g = 0$  in the paramagnetic phase. The fixed point  $h_c$  is found by the intersection of the  $g(h)$  curves for various  $L$ . Some caution should be used with this method, as the magnetization exponent is small, so that the sample distribution of  $m$  is bimodal for even large samples near the transition. The assumptions of Gaussian behavior about the mean in the paramagnetic phase are difficult to achieve. Nonetheless, the plots of  $g(h)$  show a consistent behavior that indicates the finite-size trends in the data for the magnetization. The plot of  $g(h)$  for  $L = 4$  through  $L = 64$  is shown in Fig. 2. For smaller system sizes, about  $5 \times 10^4$  ground states were found; for the  $L = 64$  systems near  $h_c$ , about

$5 \times 10^3$  ground states were computed. The apparent intersection point is  $g_c \approx 0.975$ , but this quantity likely has not converged to its scaling value. The location of the transition can be assigned with more certainty to the range  $h_c = 4.179 \pm 0.002$ . This is an acceptable value for the set of lengths used here and likely will continue to hold for scales that are somewhat larger. It is also quite consistent with the scaling of the stiffness, location of the specific heat peaks, and the algorithmic slowing down discussed in the other sections of this paper.

### B. Magnetization

The ratio of the magnetization exponent  $\beta$  to the correlation exponent length  $\nu$  is computed from the effective finite size exponent for the magnetization. Given standard finite size scaling, the magnetization at the transi-

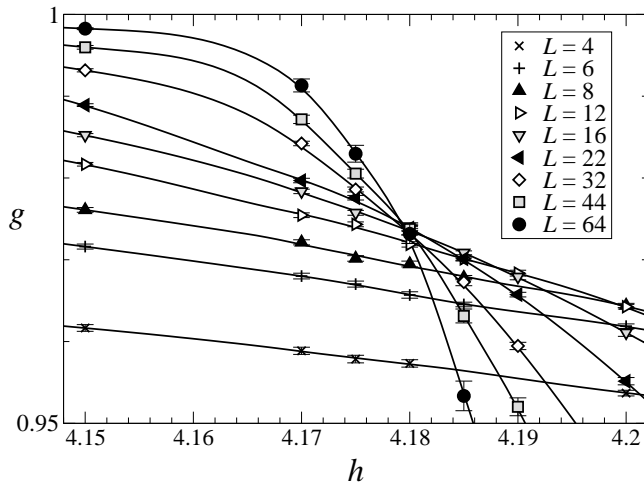


FIG. 2: Plot of the Binder cumulant  $(3 - \overline{m^4}/\overline{m^2})/2$  as a function of  $h$  for various  $L$ . The curves are smoothed spline fits to indicate the trends. This plot is used to determine the location of the transition,  $h_c = 4.179(2)$ .

tion will scale as  $m(h_c) \sim L^{-\beta/\nu}$ . The local exponent  $\beta/\nu$  is found by the discrete derivative of  $\ln(\overline{m})$  with respect to  $\ln(L)$ . The results of this computation are plotted in Fig. 3. This evaluation gives a location for the transition that is consistent, but slightly less precise, than the Binder cumulant analysis. The value of the local exponent that is most consistent with a constant value gives the estimate

$$\beta/\nu = 0.19 \pm 0.03. \quad (3)$$

In Fig. 4, the scaled magnetization (for the same samples used to compute  $g(h)$ ) is plotted as a function of scaled distance to the transition, in agreement with the finite-size scaling form

$$\overline{m} = L^{-\beta/\nu} f_m[(h - h_c)L^{1/\nu}], \quad (4)$$

where the value  $\nu = 0.83$  gives the best scaling collapse, with fixed  $\beta/\nu = 0.19$  and  $h_c = 4.179$ . The value of  $\nu$  in Table I indicates the range of values found by distinct estimates; there is no clear best measurement of  $\nu$  in the data.

### C. Fluctuations in the magnetization

In addition to the scaling of the mean magnetization, the fluctuations in the magnetization can be checked for consistency with finite-size scaling. The sample-to-sample fluctuations  $\Delta_M$  in the total magnetization  $|M| = N|m| = \sum_i s_i$  can be estimated, using the number of independent volumes and the fluctuations in the magnetization of such volumes. Defining the finite size scaling variable  $x = (h - h_c)L^{1/\nu}$ , at large  $|x|$ , the relevant volumes are of size  $\xi \sim (h - h_c)^{-\nu}$ , while at small  $|x|$ , the volume is finite-size limited. The fluctuations in

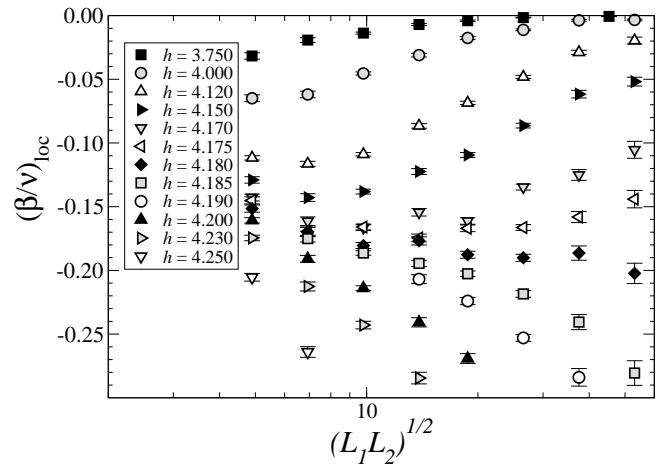


FIG. 3: Plot of estimates for  $\beta/\nu$  found from the discrete derivative  $(\beta/\nu)_{\text{loc}} = \ln(\overline{m}(h, L_2)/\overline{m}(h, L_1))/\ln(L_2/L_1)$ . The apparent convergence to a uniform value for  $h \approx 4.18$  implies that the value  $\beta/\nu = 0.19(3)$  accurately describes the effective critical behavior for  $L \approx 12 \rightarrow 64$ .

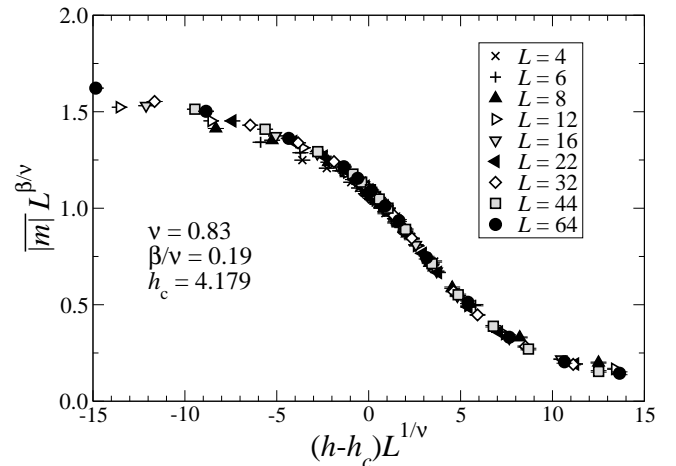


FIG. 4: Scaled magnetization  $\overline{m}L^{\beta/\nu}$  as a function of scaled disorder  $(h - h_c)L^{1/\nu}$  for  $\beta/\nu = 0.19$  and  $\nu = 0.83$ .

the magnetization over a volume  $\ell^d$  are  $M_\ell \sim \ell^{d-\beta/\nu}$  and the number of such volumes is  $n_\ell \sim (L/\ell)^d$ . Taking fluctuations over each volume to be independent, one can write a version of the scaling as

$$\Delta_M \sim M_\ell \sqrt{n_\ell} \sim L^{d/2} (h - h_c)^{d\nu/2 - \beta} f_\Delta(x), \quad (5)$$

where in the limit of large  $|x|$ ,  $f_\Delta$  approaches a constant whose value depends on the sign of  $|x|$ . For small values of  $|x|$ ,  $f_\Delta(x) \sim |x|^{-\beta+d\nu/2}$ . This scaling form is verified by the data displayed in Fig. 5. The data at small  $|x|$  is roughly consistent with the range of power laws  $-\beta + d\nu/2 \approx 1.48 \pm 0.15$  plotted in Fig. 5 (this comparison is rather sensitive to the location of  $h_c$  and the value of  $\nu$ .) At large  $|x|$ ,  $\Delta_M L^{-d/2} (h - h_c)^{\beta-d\nu/2}$  approaches a constant.

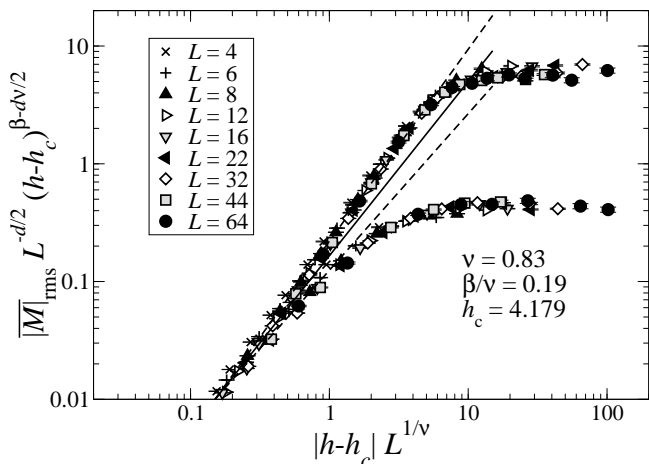


FIG. 5: Plot of the scaled fluctuations in the magnitude of the magnetization  $|M|$ . The scaling variable  $|h - h_c|L^{1/\nu}$  on the horizontal axis is the scaled distance to the critical point while the vertical axis variable,  $|M|_{\text{rms}}L^{-d/2}(h - h_c)^{d\nu/2 - \beta}$  is the magnitude of the fluctuation in the magnetization, normalized by the expected number of correlation volumes and the magnetization of the correlation volumes of linear size  $\xi \sim (h - h_c)^{-\nu}$ . The approach to a constant value at large scaling variable is consistent with independently oriented regions for  $h > h_c$  (upper branch) and magnetization fluctuations about the ferromagnetic state over regions of size  $\xi$  when  $h < h_c$  (lower branch.) The solid line represents a power law exponent  $-\beta + d\nu/2 \approx 1.48$ , while the upper (lower) dashed line has slope 1.63 (1.33.)

#### IV. HEAT CAPACITY

The specific heat of the 3D RFIM is a quantity that can be measured experimentally, directly<sup>22,23</sup> or indirectly.<sup>23,24</sup> The divergence of the specific heat has also been estimated numerically, though not all estimates agree and the experimental situation is unclear. Because of these discrepancies, it is useful to also study this quantity in the case of four dimensions, to check the validity of the standard scaling picture.

The heat capacity can be estimated using ground state calculations and applying thermodynamic relations employed by Hartmann and Young.<sup>15</sup> This approach was also applied in Refs. 16 and 25. The method relies on studying the singularities in the bond energy density

$$E_J = L^{-d} \sum_{\langle ij \rangle} s_i s_j. \quad (6)$$

This bond energy density is the first derivative  $\partial E/\partial J$  of the ground state energy with respect to  $h$  (equivalently, up to constants, with respect to  $J$ .) The derivative of the sample averaged quantity  $\overline{E}_J$  with respect to  $h$  then gives the second derivative with respect to  $h$  of the total energy and thus the sample-averaged heat capacity  $C$ . The singularities in  $C$  can also be studied by computing the singular part of  $\overline{E}_J$ , as  $\overline{E}_J$  is just the integral of  $C$  with respect to  $h$ . The finite-size scaling for the singular

part of the specific heat  $C_s$  is

$$C_s \sim L^{\alpha/\nu} \tilde{C}[(h - h_c)L^{1/\nu}], \quad (7)$$

while the scaling for the leading part (through the first singular term) of the sample averaged bond energy at  $h = h_c$  is

$$\overline{E}_{J,s}(L, h = h_c) = c_1 + c_2 L^{(\alpha-1)/\nu}, \quad (8)$$

with  $c_1$  and  $c_2$  constants.

The data analysis is based upon direct fits using  $\overline{E}_J$ . This approach avoids complications that arise in computing the uncertainties when fitting to finite-differenced estimates for  $C$ , but is otherwise equivalent to fitting to such finite differences. The fit was a least squares fit of a cubic to  $h(\overline{E}_J)$  for fixed values of  $L$ . This fit to the inverse function was more stable than fitting to  $\overline{E}_J(h)$ . The fit function was then inverted to give the estimate for  $\overline{E}_J(h)$ . The maximum slope of this estimated function is in turn used to estimate the peak in  $C(h)$  for each  $L$ . The uncertainties at any point, especially when determining the peak value  $C_{\text{max}}(L)$ , in the analysis can be estimated using a bootstrap technique (resampling the data.) The data for  $\overline{E}_J$  are plotted directly in part (a) of Fig. 6. The samples used were the same as used for the magnetization and Binder cumulant analysis. The derivatives of the fit are plotted in part (b) of this figure and compared with the heat capacity values determined by finite differencing. Note that the finite differenced values are relatively noisy due to the differentiation. This apparent noise can be reduced by less refinement in the values of  $h$  sampled, but this would reduce the resolution in  $C(h)$  and the location of the peak in  $C$ . By directly fitting to  $\overline{E}_J$  rather than the finite differences, this complication is reduced (but could be managed with appropriate care in the error analysis.)

The estimates for the maximum values of the heat capacity are plotted as a function of  $L$  in Fig. 7(a). The relatively precise data are not consistently fit by a power law until  $L > 16$ . The fit for these values gives  $\alpha/\nu = 0.31 \pm 0.04$ , where the errors are purely statistical. Given the short range of the fit (from  $L = 22$  to  $L = 64$ ), one must allow for the possibility of corrections to scaling giving a different value at larger system sizes (possibly slightly lower.) A fit of these data to  $C_{\text{max}} \sim \ln(L)$  is less successful, however (see the inset in Fig. 7(a).) As always, it is difficult to distinguish a logarithmic behavior, suggested for  $C_{\text{max}}$  in Ref. 25, from a small-power-law behavior. In Fig. 7(b), the local discrete derivatives are plotted for the cases where the behavior should be a power law (main part of the figure) and logarithmic (inset.) The power law does seem to be more consistent with a convergence to a fixed slope for this range of sizes. Though the fits are not definitive, the fitted power law behavior is most consistent with scaling relations and other data and does seem to explain the computed singularity in the bond part of the energy.

The specific heat can also be used to infer  $\nu$ . This can be done directly through scaling the widths of the

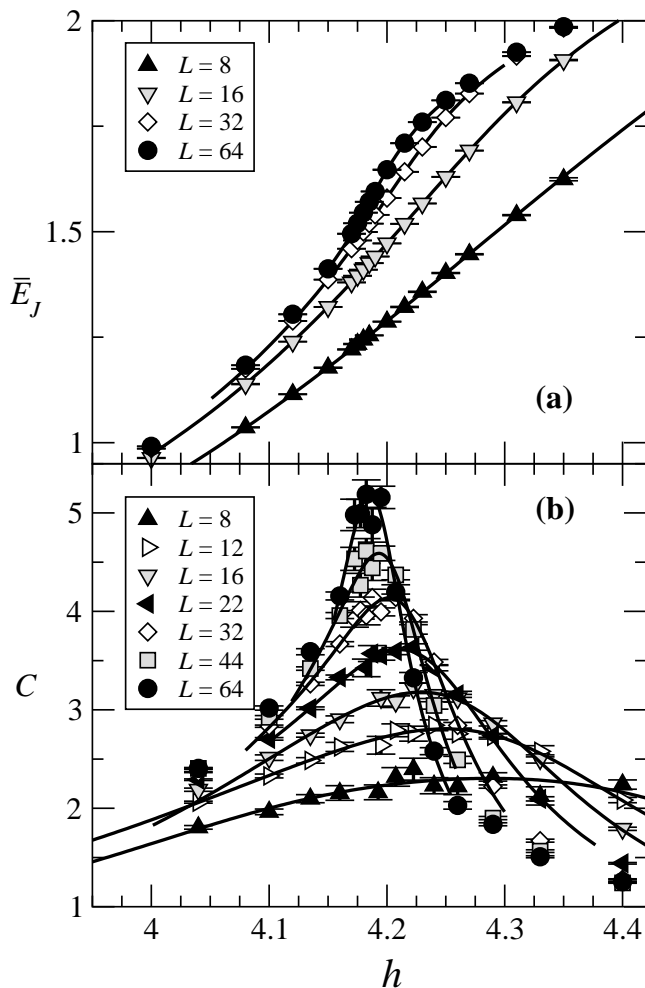


FIG. 6: (a) The points show the computed dependence of  $\bar{E}_J$ , the number density of broken bonds, on  $h$ , for  $L = 4 \dots 64$  (not all  $L$  values are included, for clarity.) Fits to cubics for the inverse function  $h(E_J)$  are shown. (b) Estimated heat capacity  $d\bar{E}_J/dh$ , derived from the differences between the  $\bar{E}_J$  values. Solid lines show the derivatives of the fits to  $\bar{E}_J$  defined in the text. These derivatives are used to estimate the heights of the peaks in the specific heat,  $C_{\max}(L)$ .

peaks in  $C$ , but a more robust procedure was to use the indirect procedure of fitting  $\bar{E}_J$ , which, being the integral over  $h$  of  $C$ , incorporates the width of the peak in  $C$ . The quantity  $(\alpha - 1)/\nu$  was found by using the fitted value of  $\bar{E}_J$  at  $h_c$ . The derivative of  $\bar{E}_J(h_c)$  with respect to  $\ln(L)$  gives the power law  $(\alpha - 1)/\nu = -0.94 \pm 0.06$ . With the value for  $\alpha/\nu$ , this gives the estimate  $\nu = 0.80 \pm 0.06$ .

## V. STIFFNESS & DOMAIN WALLS

The nature of responses to external perturbations is used to characterize distinct phases, in general. One of the more important responses to study is the response to changes in the boundary conditions. For example, ferromagnetic phases in pure materials can be identified due

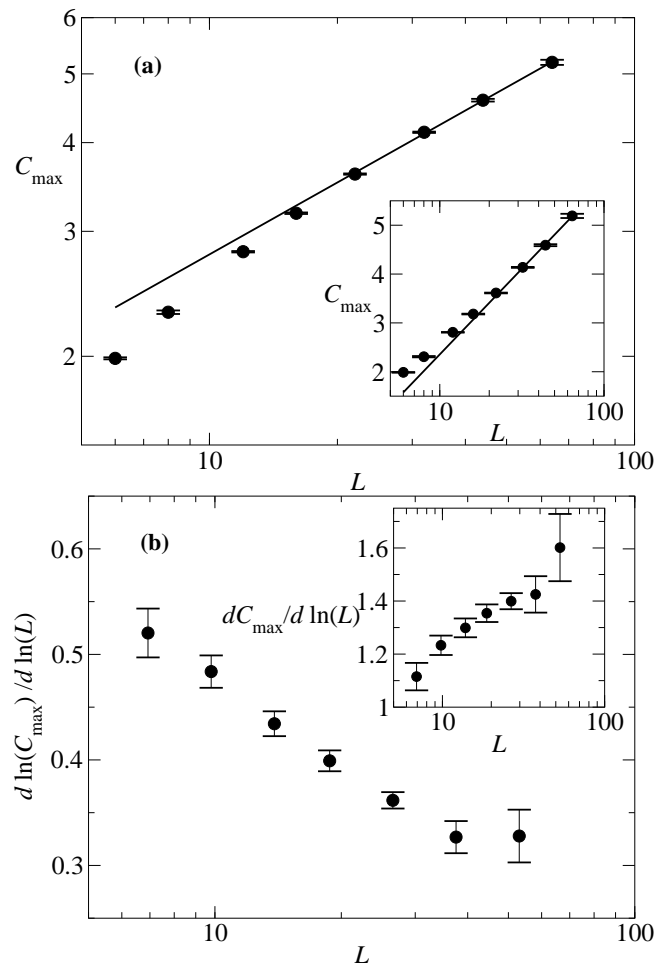


FIG. 7: (a) Plot of  $C_{\max}(L)$  vs.  $L$ . The solid line is a fit to the finite size scaling form  $C_{\max}(L) \sim L^{-\alpha/\nu}$ , with  $\alpha/\nu = 0.31 \pm 0.04$ . The inset shows a semi-log plot with a least-squares fit to the last 3 data points ( $L \geq 32$ .) (b) Local derivatives of the plots in (a).

to the finite energy density of domain walls induced by twisted boundary conditions. The application of twisted boundary conditions to stiffness and domain walls to disordered systems was introduced for spin glasses by McMillan<sup>26</sup> and Bray and Moore.<sup>27</sup> Stiffness and domain walls were studied for the 3D RFIM in Ref. 16. The approach taken quantities studied here for the 4D RFIM are the same, though the results are somewhat distinct in flavor from the 3D results.

Measuring the stiffness quantifies the change in energy due to a change in boundary conditions. The symmetrized stiffness is defined as

$$\Sigma = (E_{+-} + E_{-+} - E_{++} - E_{--})/2, \quad (9)$$

where  $E_{ab}$  is the ground state energy for boundary spins fixed to be  $a$  at one end of the sample and  $b$  at the other end of the sample (periodic boundary conditions are used in the other  $d - 1$  dimensions). This definition minimizes the effects of surface terms and has the value  $\Sigma = 0$  if the

two ends of the sample are “decoupled”, with the effect of the boundary conditions penetrating only a finite distance into the sample. The value  $\Sigma$  will be zero with high probability in the paramagnetic phase, for large samples, and is expected to scale as  $L^{d-1}$  in the ferromagnetic phase, for fixed  $h$ .

### A. Stiffness at criticality

The sample averaged stiffness  $\bar{\Sigma}$  is a quantity that is useful for investigating scaling and the order of the transition. Near a second order transition, the average stiffness scales with a characteristic scale  $L^\theta$ , where  $\theta$  is the “violation of hyperscaling” or stiffness exponent. The natural scaling assumption is that this stiffness varies over a scale given by the reduced disorder, giving

$$\bar{\Sigma} \approx \bar{C} L^\theta \mathcal{S}[L^{1/\nu}(h - h_c)K], \quad (10)$$

with  $\bar{C}$  and  $K$  nonuniversal constants and  $\mathcal{S}$  a function dependent on the shape of the sample. Another characterization of the distribution of stiffness over samples is  $P_0(h, L)$ , which is the probability that the stiffness will be exactly zero. As the distribution of the stiffness can be scaled at the critical point, with  $\Sigma = 0$  invariant under rescaling of  $\Sigma$  by  $L^\theta$ ,  $P_0(h_c, L)$  approaches a constant as  $L \rightarrow \infty$ , with the asymptotic value set by sample shape, disorder distribution, and lattice type. This convergence to a constant was used in Ref. 16 to locate  $h_c$  for the 3D RFIM.

The probability of zero stiffness  $P_0$  is plotted in Fig. 8, for samples of shape  $3L \times L^3$ . Less anisotropic samples had a very small value of  $P_0$  and therefore had more statistical error. As the running time for a given  $L$  is larger and the ground states for four different boundary conditions were computed, fewer samples were studied here than in the magnetization and energy study. For  $L = 32$ , up to  $5 \times 10^3$  realizations were studied, while for the smallest samples,  $E_J$  was calculated for about  $5 \times 10^4$  samples. The estimates plotted are consistent with  $P_0$  approximately constant in  $L$  for  $h_c \approx 4.18$ . This is in accord with other estimates of  $h_c$ , though the uncertainty in using this plot to determine  $h_c$  is somewhat larger than from other methods.

A scaling plot showing the collapse of the stiffness calculations for samples of the same shape,  $3L \times L^3$ , is shown in Fig. 9. Assuming the scaling form Eq. (10), a collapse to a single function should be found when plotting  $\bar{\Sigma} L^{-\theta}$  as a function of  $(h - h_c)L^{1/\nu}$ . This collapse is unreasonably good (that is, is not too bad for  $L = 6$ ), using  $h_c = 4.177$ ,  $\theta = 1.82$  and  $\nu = 0.80$ . The computations strongly support the picture of a second order transition with a value for  $\theta$  obeying the bounds<sup>18–20</sup>

$$d/2 - \beta/\nu \leq \theta \leq d/2. \quad (11)$$

When  $d = 3$ , it has not been possible to determine whether  $\theta \neq d/2$ , given that  $\beta/\nu$  is so small. Here, given

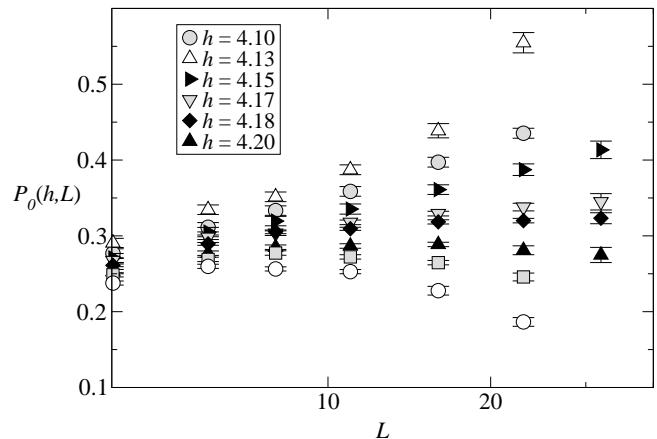


FIG. 8: Plot of the probability of zero stiffness  $\Sigma$ . The samples have a cross section volume of  $L^3$  with a distance of  $3L$  between the controlled faces. The probability is constant to within numerical errors for  $h \approx 4.18$ .

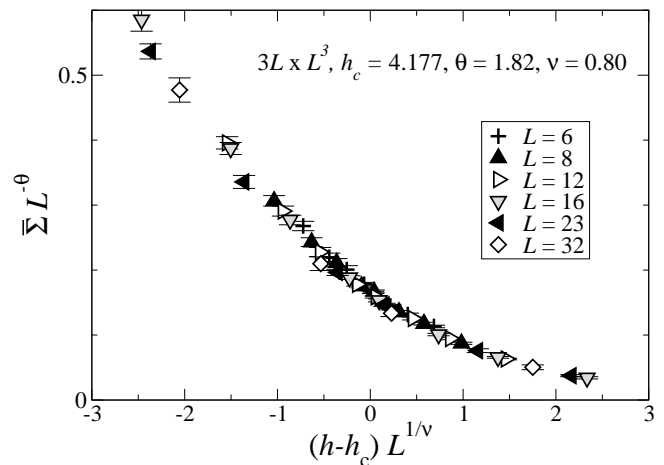


FIG. 9: Scaling plot for the stiffness. The samples have a cross section volume of  $L^3$  with a distance of  $3L$  between the controlled faces. The scaled stiffness  $\bar{\Sigma} L^{-\theta}$  is plotted vs. the scaled disorder  $(h - h_c)L^{1/\nu}$  for the values  $\theta = 1.82$  and  $\nu = 0.80$ .

the larger value of  $\beta/\nu$ , it is possible to discriminate between  $\theta$  and  $d/2$ , with the result suggesting that  $\theta < d/2$  (in addition, the result is consistent with saturation of the lower bound.)

### B. Domain walls

The calculations for the set of boundary conditions  $++$ ,  $--$ ,  $+-$ , and  $-+$  on the two opposite controlled faces (separated by  $3L$ ) have also been used to study the domain walls in the 4D RFIM. Following the definitions of Ref. 16, three definitions of the domain wall are considered. The first is found by comparing  $++$  and  $+-$  boundary conditions, with the spins fixed to be  $+$  on the left end in both cases. The set of spins which is

connected to the left end and fixed under both sets of boundary conditions has an internal boundary that intersects  $W_s$  bonds. Assuming scaling at  $h_c$ , the surface measure scales as

$$\overline{W}_s \sim L^{d_s}, \quad (12)$$

defining the domain-wall dimension  $d_s$ . The next domain-wall measure exponent is found by comparing the  $+-$  configuration with the  $--$  and  $++$  configurations. The number of bonds which are unsatisfied only with  $+-$  boundary conditions gives a domain wall measure  $W_I$ . Under  $--$  and  $++$  boundary conditions, there are unsatisfied bonds due to frozen spin regions, where the random field is strong enough to fix the spins under all boundary conditions. The unsatisfied bonds with either of these two boundary conditions are not counted as part of the  $+-$  domain wall under this definition. The only broken bonds which are counted as part of  $W_I$  are those broken due to the twisted boundary conditions. This measure similarly defines an incommensurate surface exponent by

$$\overline{W}_I \sim L^{d_I}. \quad (13)$$

The third definition of the effect of boundary conditions is given by the bond or exchange part of the stiffness,

$$\Sigma_J = (E_{+-}^J + E_{-+}^J - E_{++}^J - E_{--}^J)/2, \quad (14)$$

where  $E_J = J \sum_{\langle ij \rangle} s_i s_j$ . This count includes some broken bonds with negative sign and is influenced by frozen islands. The ‘‘dimension’’  $d_J$  is then

$$\overline{\Sigma}_J \sim L^{d_J}. \quad (15)$$

As  $\overline{\Sigma}_J$  is the derivative of  $\Sigma$  with respect to  $J$ , thermodynamic relations<sup>16</sup> imply that

$$d_J = \theta + \frac{1}{\nu}. \quad (16)$$

The values of  $d_s$ ,  $d_I$  and  $d_J$  were estimated by taking the discrete logarithmic derivatives of  $\overline{W}_s$ ,  $\overline{W}_I$  and  $\overline{\Sigma}_J$ ,

$$d_{s,I,J}(\sqrt{L_1 L_2}) = \ln[W(L_2)/W(L_1)]/\ln(L_2/L_1), \quad (17)$$

with  $W$  being one of the measures of the domain wall. The results are plotted in Fig. 10.

One of the more striking differences between the 3D and 4D calculations is that, while  $d_s \neq d$  in 3D, when  $d = 4$  the value of  $d_s$  is consistent with the relation

$$d_s = d. \quad (18)$$

Thus, the domain wall defined by the surface of connected fixed spins anchored at the fixed end of the sample has dimension consistent with the spatial dimension. This surface, the internal boundary between flipped and fixed spins, appears to be space-filling. Additionally, the estimated value of  $d_I = 3.20 \pm 0.12$  is clearly distinct from  $d_s$ , in contrast with the near equality seen in 3D.<sup>16</sup> These differences will be addressed in more detail in Sec. VI, when examining the frozen spins for  $h < h_c$ .

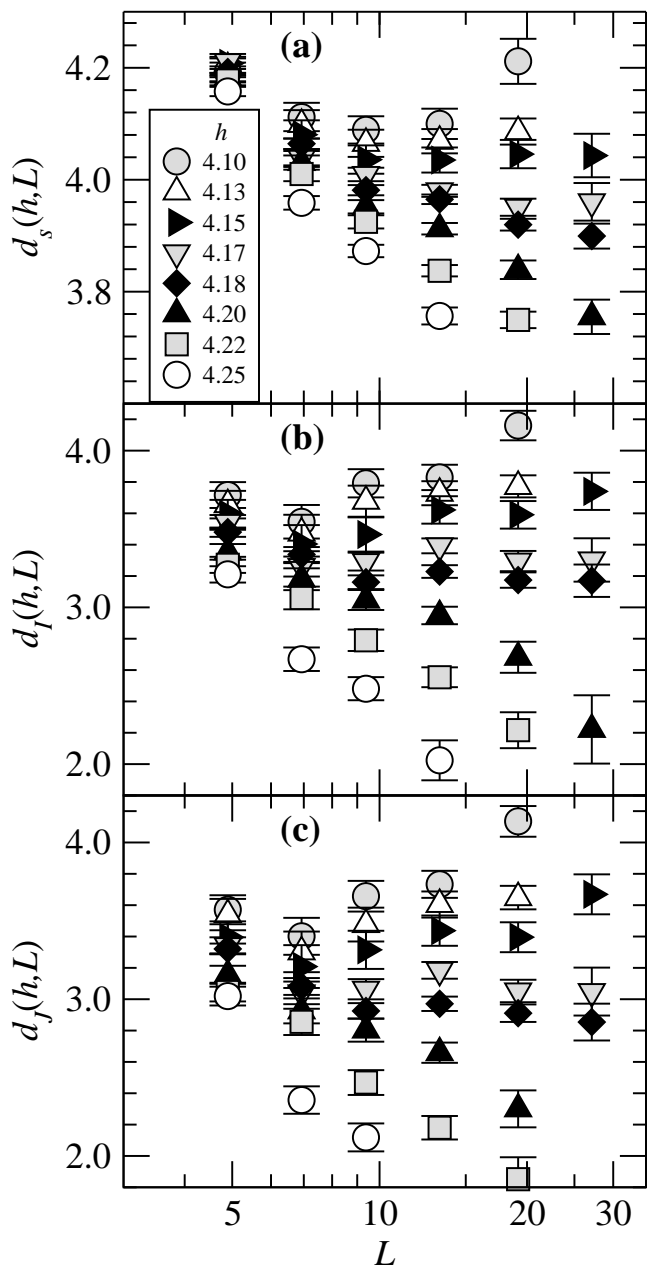


FIG. 10: Estimate of the dimensions (a)  $d_s$ , (b)  $d_I$ , and (c)  $d_J$  obtained from the discrete logarithmic derivatives of wall area  $\overline{W}_s$ , the number of bonds  $\overline{W}_I$  created by twisted BC's relative to uniform sign BC's, and the exchange stiffness  $\overline{\Sigma}_J$  with respect to  $L$  for several  $h$ . These plots are used to infer  $d_s = 3.94 \pm 0.06$ ,  $d_I = 3.20 \pm 0.12$  and  $d_J = 2.94 \pm 0.12$ .

### C. Domain walls and scaling

The value computed here for  $d_J$ ,  $d_J = 2.94 \pm 0.12$ , is just consistent with Eq. (16). As the derivation of Eq. (16) is quite robust, this consistency should not be surprising. Though the arguments are apparently sound, the conjecture made originally for 3D,<sup>16</sup> namely that

$$d_I = d_J + \beta/\nu, \quad (19)$$

has a non-rigorous derivation, especially as in the above form,  $d_s$  in the original version has been replaced by  $d_I$ , which here more clearly reflects the measure of the domain walls induced by boundary condition changes. However, this scaling relation is easily consistent with the computed values of the domain wall exponents and  $\beta/\nu$ .

The value found here for  $(\alpha - 1)/\nu$  also satisfies the relationship  $d_I - d - \beta/\nu = (\alpha - 1)/\nu$ , which was used in Ref. 16, except for the replacement here of  $d_s$  by  $d_I$ , motivated in the 4D RFIM by the more natural definition of domain walls using  $d_I$  and the spatial structure of frozen spins.

## VI. FROZEN AND MINORITY SPINS

The result that one measure of the domain wall dimension,  $d_s$ , is near to the spatial dimension  $d$  suggests that the picture of the spin configurations must differ between the cases  $d = 3$  and  $d = 4$ . The picture of the configuration at the transition in  $d = 3$  described in Ref. 16 is that of nested domain walls, where the domain walls are the boundaries separating connected sets of spins of the same sign (see also Ref. 19.) In this section, results are presented that necessitate a different picture in  $d = 4$ , due to the percolation of minority spins for  $h$  less than the critical disorder  $h_c$ . (These results should be compared with those for the 3D RFIM presented in Ref. 28, which support the existence of two interpenetrating spanning domains in the 3D RFIM for  $h > h_c$ , and those of Ref. 29, where the surprising claim is made that there is a second critical  $h_p > h_c$  where there is first simultaneous spanning by up and down spin clusters.) The percolation of minority spins in  $d = 4$  for  $h < h_c$  makes the identification of domain walls with connected sets of uniform spins problematic.

Given a disorder realization  $\{h_i\}$ , there are two natural sets of spins to consider when defining domain walls and percolation clusters. The minority spins are simply those that have spin opposite to the mean magnetization. The fraction of spins that fall into this category is  $(1 - |m|)/2$ . Frozen spins are those that are invariant under all boundary conditions. These spins are minority spins under either all up or all down boundary conditions, so that the fraction of frozen spins is  $1 - |m|$ , when  $L \gg \xi$ . If either minority or frozen spins were distributed independently in space, the clustering of these spins would map directly onto simple percolation. As there are strong interactions between these spins and the boundaries between them are related to domain walls, the percolation is not simple, on short length scales. For  $h < h_c$ , the correlations should vanish in the limit of separations much greater than  $\xi$ .

The clustering and percolation behavior of these spins can be directly studied to learn more about the domain walls. From ground state configurations for  $L = 8$  through  $L = 64$ , computed both for all up and all down

boundary spins, the frozen and minority spin sets were identified. These sets can be studied directly or in a coarse grained sense. (Coarse grained spin blocks were determined by whether the minority or frozen spins were a majority of the block, with ties randomly broken.) The spanning clusters were defined as those that connected two opposite faces of the hypercubic sample.

Fig. 11 is a plot of the percolation probability  $p_b$  (i.e., the probability of at least one spanning cluster) of minority spins on scales  $b = 1, 2, 4$  as a function of  $h$ . From this plot, an extrapolation of the curve crossings to large  $L$  suggests that the minority spins percolate in the infinite-volume limit at  $h_p^m = 3.850 \pm 0.005$ . Plots for the frozen spins are qualitatively similar, with a lower percolation threshold of  $h_p^f = 3.680 \pm 0.005$ . In each case, the number of spanning clusters peaks near  $h_p^{m,f}$ , with the peak number increasing with  $L$ . The percolation point tends toward  $h_c$  as the scale  $b$  increases, consistent with a scaling toward the ferromagnetic state of uniform magnetization for  $h < h_c$ .

Implications for the simple domain wall picture in  $d = 4$  follow directly. As the minority spins percolate in the ferromagnetic phase,  $h < h_c$ , the boundaries of connected sets of same-sign spins are space filling. The definition of domain walls using simply these connected sets is thus not clearly informative about the effect of boundary condition changes. The surfaces defined by the incongruent bonds are more useful in understanding the domain walls. These are the surfaces that separate the two ferromagnetic ground states; the frozen spins make a space-filling background that is common to both states, even for  $h < h_c$ . (In three dimensions, at  $h = h_c$ , there is a fractal set of spins that can be controlled by the boundary conditions.) In addition, the relationship in 3D between  $\beta/\nu$  and  $\rho_\infty$ , the probability of crossing a domain wall per factor of  $e$  in length scale, would be much more difficult to investigate in 4D, as the domain walls are not readily identifiable.

## VII. STATES

In earlier sections, it has been (sometimes implicitly) assumed that the transition in the 4D RFIM is consistent with the simple picture of a ferromagnetic to paramagnetic transition, with the sign of the magnetization in the ferromagnetic state dependent on boundary conditions and the spin configuration independent of boundary condition in the paramagnetic state, far from the boundaries. This assumption is examined in this section. The approach is inspired in large part by analytic work.<sup>30,31</sup> A discussion of the numerical study of the nature of the thermodynamic states is presented in Ref. 21 and the applications to the 3D RFIM can be found in Ref. 16. In summary, one test of the number of states in the thermodynamic limit is to determine the correlation functions (in this case, the ground state) in the interior of the sample under several different boundary conditions. For a

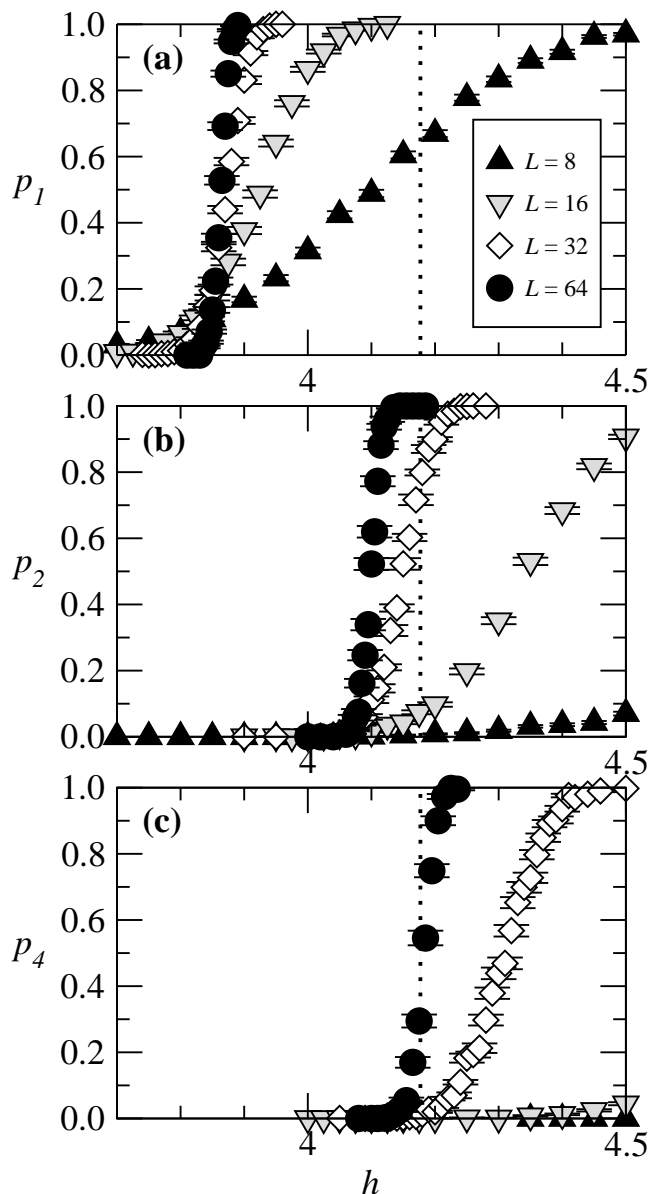


FIG. 11: Plot of the percolation probability for minority spins as a function of disorder strength  $h$ , for  $L = 8, 16, 32, 64$ . The dashed line indicates  $h = h_c$ . (a) Percolation probability  $p_1$  for minority spins. The percolation probability approaches unity for large systems for  $h_p^f = 3.875 \pm 0.005$ . (b) Percolation probability  $p_2$  for minority block spins of size  $2^4$ . The percolation threshold is closer to  $h_c$ . (c) Percolation probability  $p_4$  for minority block spins of size  $4^4$ .

small number (one or two for Ising models) of thermodynamic limits, there will be a small number of interior configurations. The probability that the interior of the ground states will differ from one of the large volume limit configurations decreases as a power law dependent on the dimension of the domain wall.

The degeneracy of the ground state was directly addressed for the 4D RFIM by studying the effect of changing boundary conditions on the ground state spin config-

uration in the interior of the sample. In particular, the periodic ( $P$ ), all spins up ( $+$ ), all spins down ( $-$ ), and open ( $O$ ) boundary conditions were compared. As the 4D computations are much more time consuming, the comparison between the ground states of a system and a smaller subsystem, each with open boundary conditions, was not extensively studied, as it was in the 3D RFIM.

A summary of the results for comparisons between  $P$  and  $+/-$  is presented in Figs. 12 and 13. The results for  $O$  vs.  $+/-$  are quite similar. The plots show the (scaled) probability  $P_{P,+/-}(2, h, L)$ , for a given  $h$  and  $L$ , that the ground-state  $P$  configuration is distinct from both the ground-state  $+$  and  $-$  configurations in the central volume of size  $2^4$ . As  $L$  increases, this probability decreases toward zero at all  $h$ . This suggests that in large samples, the interior configuration for a number of boundary conditions (including periodic and open) can be found by imposing either  $+$  or  $-$  boundary conditions. It was also found, as in the 3D case, that for  $h > h_c$ , as  $L$  increases, the interior configurations for the  $+$  and  $-$  boundary conditions become identical with unit probability. Together, assuming the extrapolation to large  $L$  is correct, these results show the existence of a single state for  $h > h_c$  (for if the interior configuration differs between *any* two boundary conditions, it must differ between  $+$  and  $-$ ) and strongly suggest the existence of only two states for  $h < h_c$ .

The scaling of  $P_{P,+/-}$  is consistent with previous work on disordered models.<sup>21,32</sup> As a function of the scaled disorder  $(h-h_c)L^{1/\nu}$ , the function approaches a single curve when the probability  $P_{P,+/-}$  is scaled by  $L^{d-d_I}$ . This scaling results from assuming that the number of large (size  $L$ ) domain walls induced by generic boundary condition changes is constant as  $L \rightarrow \infty$ . This assumption is consistent with the observation that  $d_I > d-1$ . The chance that an interior volume of fixed linear size  $w$  intersects a domain wall is expected to behave as  $(w/L)^{d-d_I}$ . The clean collapse of the data for larger system sizes, using values determined from magnetization and domain wall measurements, lend quantitative support to this picture.

The dimension  $d_I$  could be alternatively deduced from this data. Fig. 14 shows the dependence of the peak value of  $P_{P,+/-}$  on  $L$ . Assuming  $d-d_I$  gives this slope, the data for  $L = 12 \rightarrow 44$  gives  $d_I = 3.19(2)$ . This value could be taken as the best one for  $d_I$ , but this is not done here and is instead used as a confirmation of the scaling picture.

## VIII. ALGORITHMIC SLOWING DOWN

In the 3D RFIM, it was found that the number of operations carried out by the ground state algorithm diverged near the ferromagnetic-paramagnetic transition. In this section, similar results are presented for the 4D RFIM. The scaling results here have greater accuracy near the transition. The scaling is found to be quite consistent with the heuristic picture presented in Ref. 33.

The key quantitative relation to be elucidated is that

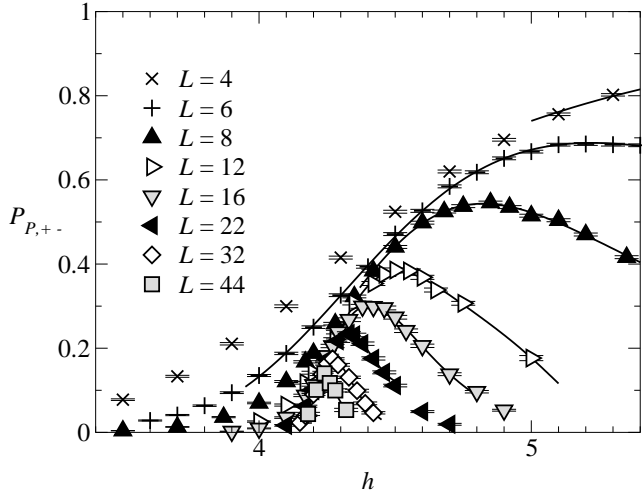


FIG. 12: Plot of  $P_{P,+}(-2, h, L)$ , the probability that, at given sample size  $L$  and disorder  $h$ , the ground state with periodic boundary conditions will differ from ground state configurations for both fixed  $+$  and  $-$  boundary conditions, in a volume of size  $2^4$  in the center of the volume  $L^4$ . Note that extrapolating to  $L \rightarrow \infty$  suggests that  $P_{P,+}(-2, h, L) \rightarrow 0$  for all  $h$ . The solid lines are least-squares fits to quartics in  $\ln(P)$ .

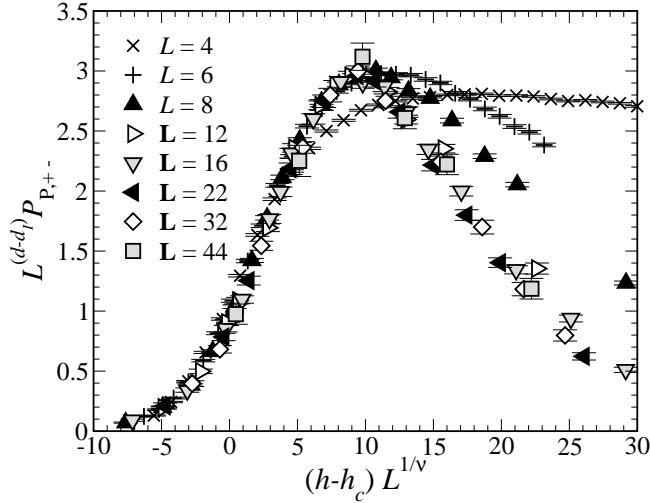


FIG. 13: Scaling plot for  $P_{P,+}(-2, h, L)$ , using the scaled probability  $P_{P,+} L^{d-d_I}$  and scaled disorder  $(h-h_c)L^{1/\nu}$ , with values  $d_I = 3.2$  and  $\nu = 0.8$ . The scaling collapse suggests that the changes in boundary conditions typically introduce a finite number of domain walls (say, one of size  $L$ ) with  $\sim L^{d_I}$  bonds at  $h = h_c$ .

between the number of primitive operations carried out to find the ground state and the physical understanding of the phase transition and correlation volumes. In Ref. 33, it was argued that the time per spin to find the ground state in the RFIM is directly proportional to the linear size  $L$  near the transition. This results from the nature of the push-relabel algorithm<sup>16,34</sup> used, which efficiently constructs a “height” field over the lattice that

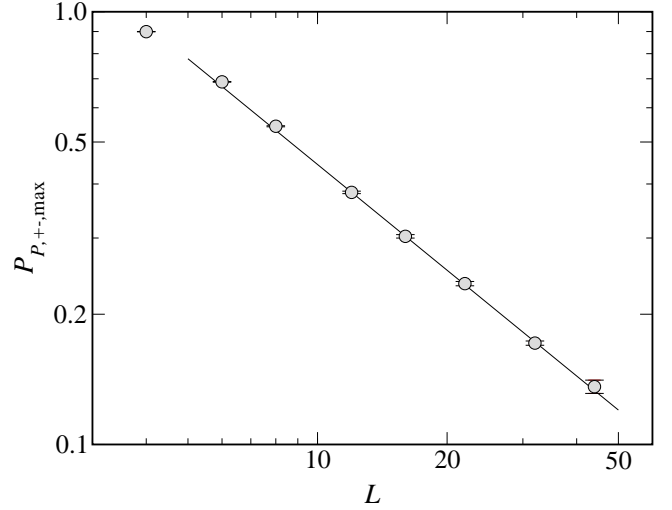


FIG. 14: Plot of the dependence of the maximum of  $P_{P,+}(-2, h, L)$  over  $h$  on the system size  $L$ . The solid line is a fit to  $P_{P,+}^{max} \sim L^{-(d-d_I)}$ , with  $d - d_I = 0.81 \pm 0.02$ .

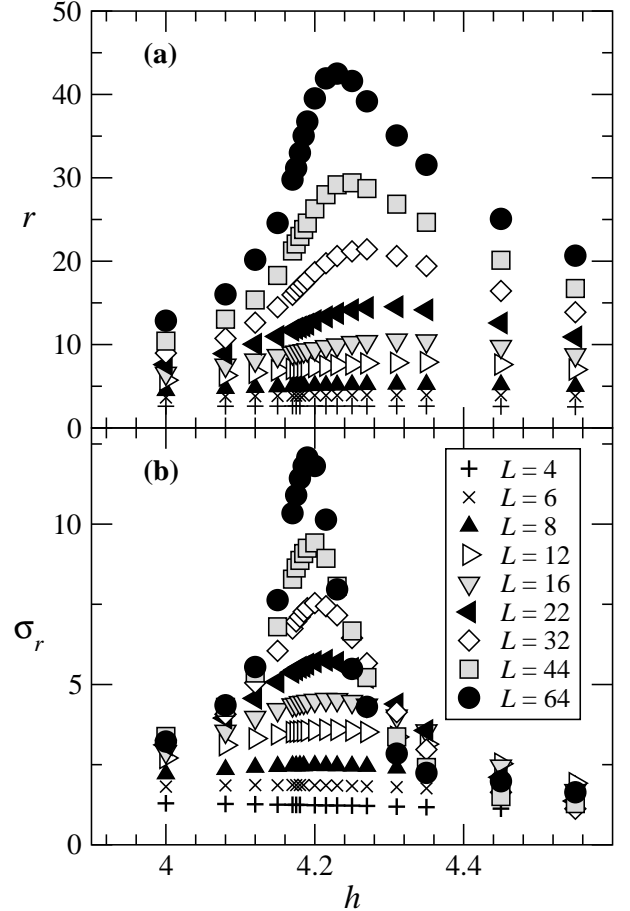


FIG. 15: (a) Plot of the number of relabel operations per spin,  $r$ , carried out by the ground state algorithm as a function of  $h$ , for  $L = 4 \dots 64$ . (b) Plot of the sample-to-sample fluctuations  $\sigma_r$  in the number of relabel operations per spin. This quantity provides an especially sharp and quickly diverging curve for estimating  $h_c$ .

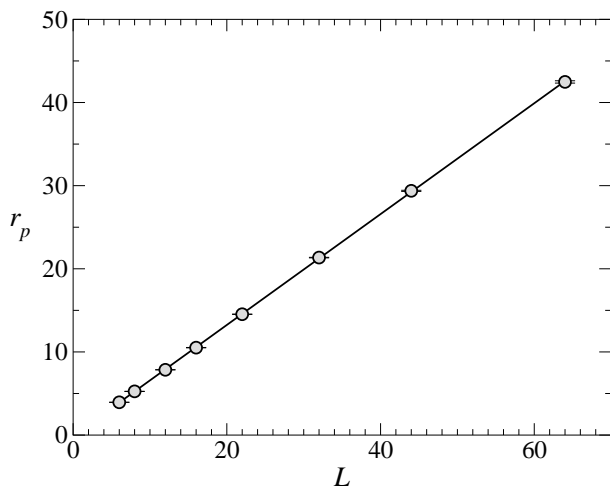


FIG. 16: Linear plot of the height of the peak  $r_p(L)$  in  $r$  vs.  $h$ . The value of  $r_p$  scales almost exactly linearly with  $L$ .

guides the “flow” (corresponding to the redistribution of excess “fluid” or external magnetic field  $h_i$ .)

The relabel operation is one of the primitive operations carried out during the convergence of the algorithm to the physical ground state. In Fig. 15, the sample average  $r$  of the number of relabel operations per spin and the sample-to-sample fluctuations in  $r$ ,  $\sigma_r$ , are plotted as a function of  $h$  for different  $L$ . (Results for the number of the other primitive operations, the push operations, are quite similar.) There is clearly a peak in both quantities near  $h_c$ , with the peak in the sample-to-sample fluctuations being more sharply peaked, relative to the non-critical contribution<sup>35</sup>.

The  $r(h)$  curves were fit with fourth-order polynomials to extract the peak value  $r_p(L)$ . The plot of this quantity is shown in Fig. 16. A linear fit is shown, which is remarkably consistent with the data over a wide range of  $L$ . The result is in agreement with the arguments of

Ref. 33 and supports the relationship between the physical correlation length and the evolution of the algorithm.

## IX. SUMMARY

By computing the ground state for a large number of samples of volume up to  $L^4 = 64^4$ , the quantitative and qualitative thermodynamic properties of the 4D RFIM have been studied. The derived exponents satisfy the conventional scaling relations. The values of the exponents and location of the transition are consistent with, but are based on larger systems than, the results for the Gaussian 4D RFIM published in Refs. 11,25. Note that, as in previous work, the value for  $\nu$  is the least certain and that errors in  $\nu$  propagate to estimates of  $\beta$  and  $\alpha$ . The picture of a single transition from a nearly-two-fold-degenerate ferromagnetic state to a single paramagnetic state is confirmed by comparing ground states with varying boundary conditions. Strong evidence is presented that the picture of domain walls developed<sup>16</sup> for the 3D RFIM must be modified to describe the 4D RFIM. In particular, the percolation of frozen and minority spins within the ferromagnetic phase implies that the sets of connected same-sign spins are not the boundaries of domain walls. The empirical running times for the ground state algorithm peak near the phase transition in a manner consistent with previous descriptions,<sup>16,33</sup> with the peak running time per spin apparently proportional to the linear system size. The algorithmic running times provide a check on the location of the transition and the scaling exponent  $\nu$ .

I would like to thank Daniel Fisher for discussions and Alexander Hartmann for communicating related work prior to its submission. This material is based on work supported by the National Science Foundation under Grant No. DMR-0109164.

<sup>1</sup> J. Z. Imbrie, Phys. Rev. Lett. **53**, 1747 (1984); Comm. Math. Phys. **98**, 145 (1985). J. Bricmont and A. Kupiainen, Phys. Rev. Lett. **59**, 1829 (1987). M. Aizenman and J. Wehr, Phys. Rev. Lett. **62**, 2503 (1989).  
<sup>2</sup> For a review, see T. Nattermann in “Spin Glasses and Random Fields”, ed. A. P. Young (World Scientific, Singapore, 1998).  
<sup>3</sup> M. Mézard and A.P. Young, Europhys. Lett. **18**, 653 (1992); M. Mézard and R. Monasson, Phys. Rev. B **50**, 7199 (1994).  
<sup>4</sup> M. S. Cao and J. Machta, Phys. Rev. B **48**, 3177 (1993).  
<sup>5</sup> H. Rieger and A. P. Young, J. Phys. A **26**, 5279 (1993).  
<sup>6</sup> H. Rieger, Phys. Rev. B **52**, 6659 (1995), cond-mat/9503041.  
<sup>7</sup> M. E. J. Newman and G. T. Barkema, Phys. Rev. E **53**, 393 (1996), cond-mat/9507044.  
<sup>8</sup> J. Machta, M. E. J. Newman, and L. B. Chayes, Phys.

Rev. E **62**, 8782 (2000), cond-mat/0006267.  
<sup>9</sup> J. C. A. d’Auriac, M. Preissmann, and R. Rammal, J. Phys. Lett. **46**, L173 (1985).  
<sup>10</sup> A. T. Ogielski, Phys. Rev. Lett. **57**, 1251 (1986).  
<sup>11</sup> M. R. Swift, A. J. Bray, A. Maritan, M. Cieplak, and J. R. Banavar, Europhys. Lett. **38**, 273 (1997), cond-mat/9705289.  
<sup>12</sup> J. C. Anglès d’Auriac and N. Sourlas, Europhys. Lett. **39**, 473 (1997), cond-mat/9704088.  
<sup>13</sup> N. Sourlas, Comp. Phys. Comm. **121**, 184 (1999), cond-mat/9810231.  
<sup>14</sup> A. K. Hartmann and U. Nowak, Eur. Phys. J. B **7**, 105 (1999), cond-mat/9807131.  
<sup>15</sup> A. K. Hartmann and P. Young, Phys. Rev. B **64**, 214419 (2001), cond-mat/0105310.  
<sup>16</sup> A. A. Middleton and D. S. Fisher, Phys. Rev. B **65**, 134411 (2002), cond-mat/0107489.

- <sup>17</sup> I. Dukovski and J. Machta, cond-mat/0207438.
- <sup>18</sup> D. S. Fisher, Phys. Rev. Lett. **56**, 416 (1986).
- <sup>19</sup> J. Villain, J. Phys. **46**, 1843 (1985).
- <sup>20</sup> M. Schwartz and A. Soffer, Phys. Rev. Lett. **55**, 2499 (1985).
- <sup>21</sup> A. A. Middleton, Phys. Rev. Lett. **83**, 1672 (1999), cond-mat/9904285.
- <sup>22</sup> J. Satooka, H. A. Katori, A. Tobo and K. Katsumata, Phys. Rev. Lett. **81**, 709 (1998), cond-mat/9801039.
- <sup>23</sup> R. J. Birgeneau, Q. Feng, Q. J. Harris, J. P. Hill, A. P. Ramirez, and T. R. Thurston, Phys. Rev. Lett. **75**, 1198 (1995).
- <sup>24</sup> D. P. Belanger, A. R. King, V. Jaccarino, and J. L. Cardy, Phys. Rev. B **28**, 2522 (1983).
- <sup>25</sup> A. K. Hartmann, cond-mat/0201441.
- <sup>26</sup> W. L. McMillan, Phys. Rev. B **30**, 476 (1984).
- <sup>27</sup> A. J. Bray and M. A. Moore, Phys. Rev. B **31**, 631 (1985).
- <sup>28</sup> J. Esser, U. Nowak, and K. D. Usadel, Phys. Rev. B **55**, 5866 (1997), cond-mat/9612022.
- <sup>29</sup> E. T. Seppälä, A. M. Pulkkinen, and M. J. Alava, cond-mat/0206376.
- <sup>30</sup> D. A. Huse and D. S. Fisher, J. Phys. A **20**, L997 (1987); D. S. Fisher and D. A. Huse, J. Phys. A **20**, L1005 (1987).
- <sup>31</sup> C. M. Newman and D. L. Stein, Phys. Rev. B **46**, 973 (1992); Phys. Rev. Lett. **72**, 2286 (1994); **76**, 515 (1996), adap-org/9508006; **76**, 4821 (1996); C. M. Newman and D. L. Stein, Phys. Rev. E **55**, 5194 (1997), cond-mat/9612097; **57**, 1356 (1998), cond-mat/9711010.
- <sup>32</sup> M. Palassini and A. P. Young, Phys. Rev. B **60**, 9919 (1999), cond-mat/9904206.
- <sup>33</sup> A. A. Middleton, Phys. Rev. Lett. **88**, 017202 (2002), cond-mat/0104185.
- <sup>34</sup> M.J. Alava, P.M. Duxbury, C. Moukarzel and H. Rieger, in *Phase Transitions and Critical Phenomena, Vol. 18*, eds. C. Domb and J. L. Lebowitz, (Academic Press, San Diego, 2001).
- <sup>35</sup> The non-critical background to  $r$  or  $\sigma_r$  may, however, have a magnitude that slowly diverges with  $L$ , as discussed in Ref. 33.

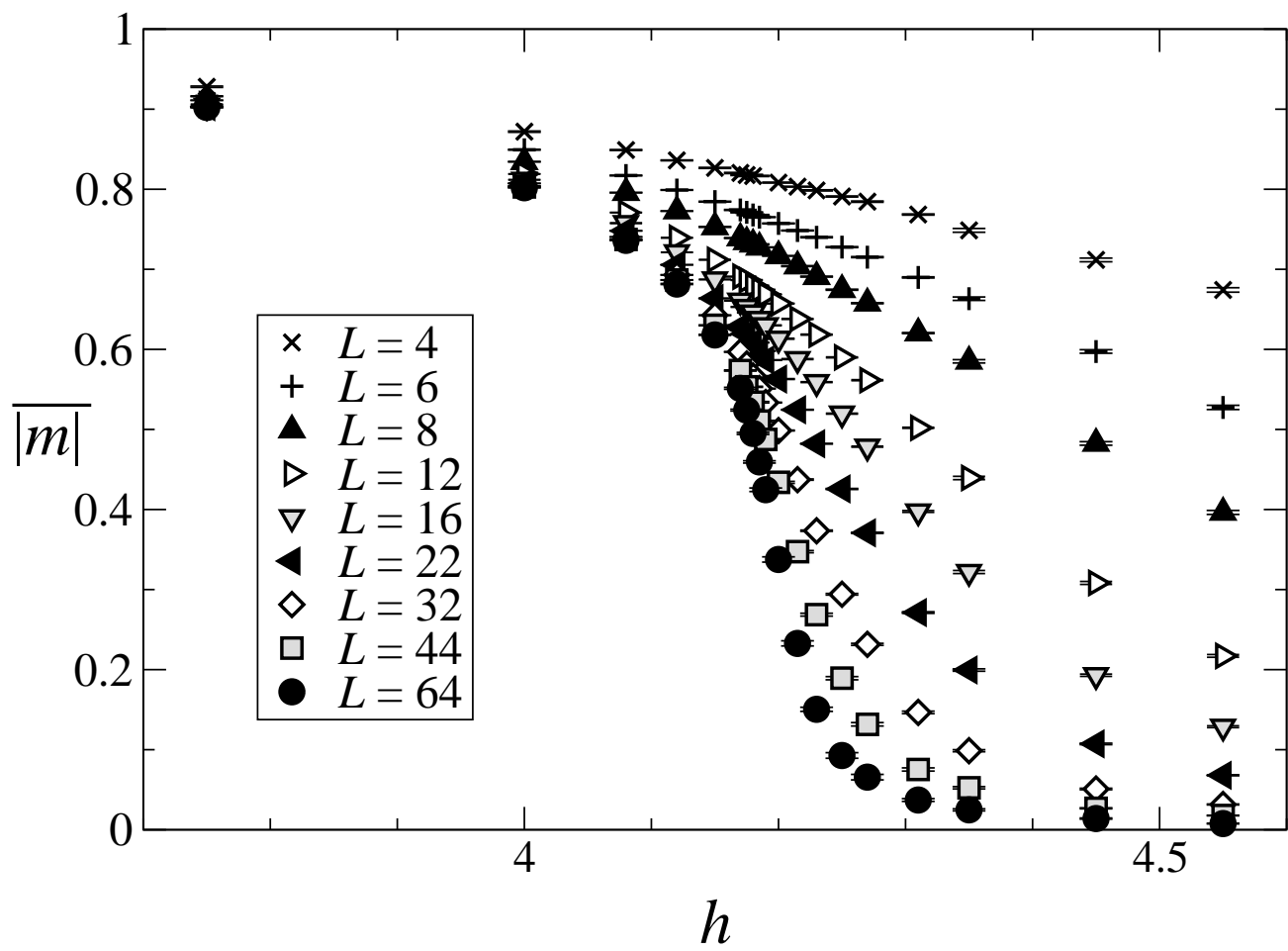


Figure 1

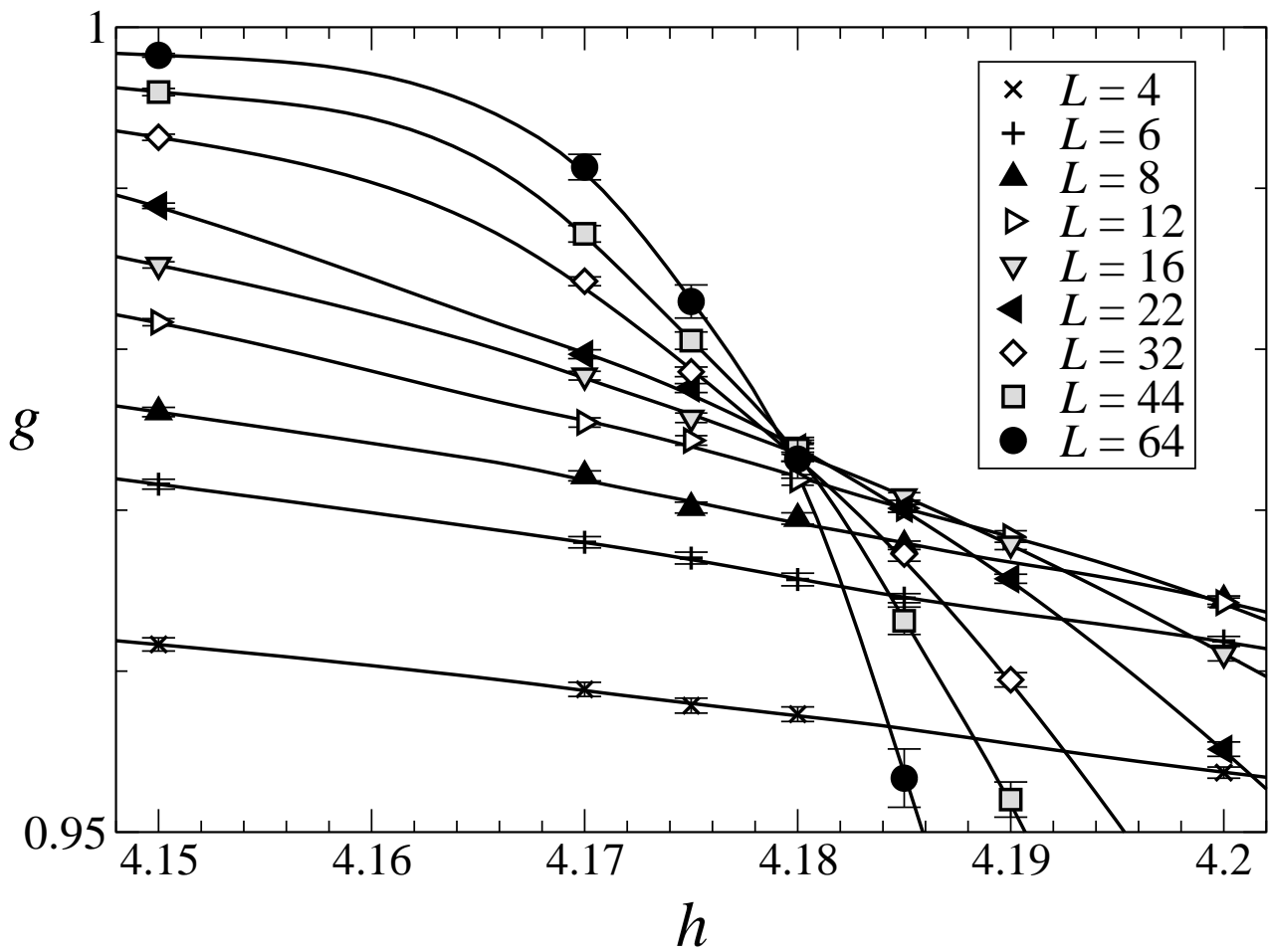


Figure 2

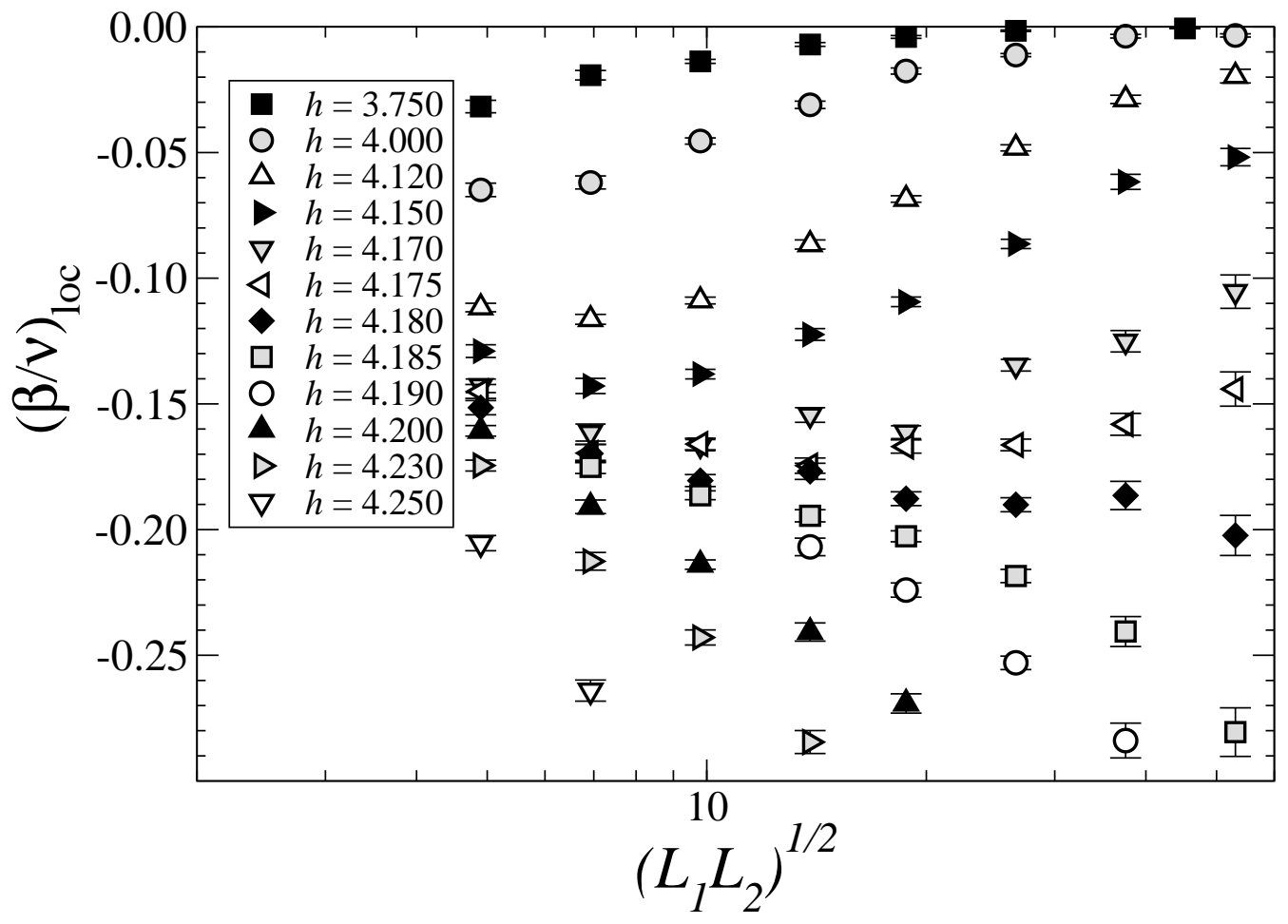


Figure 3

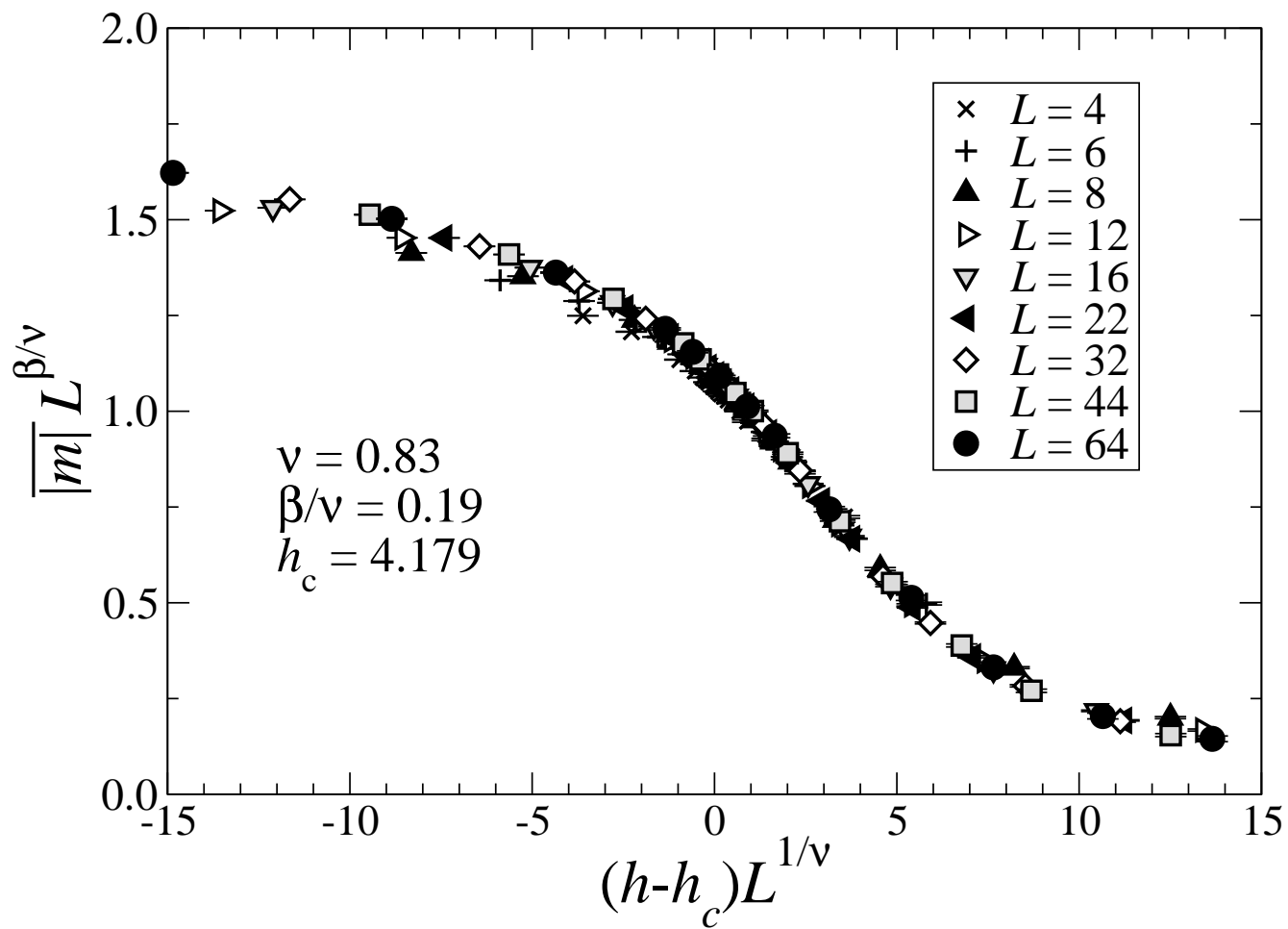


Figure 4

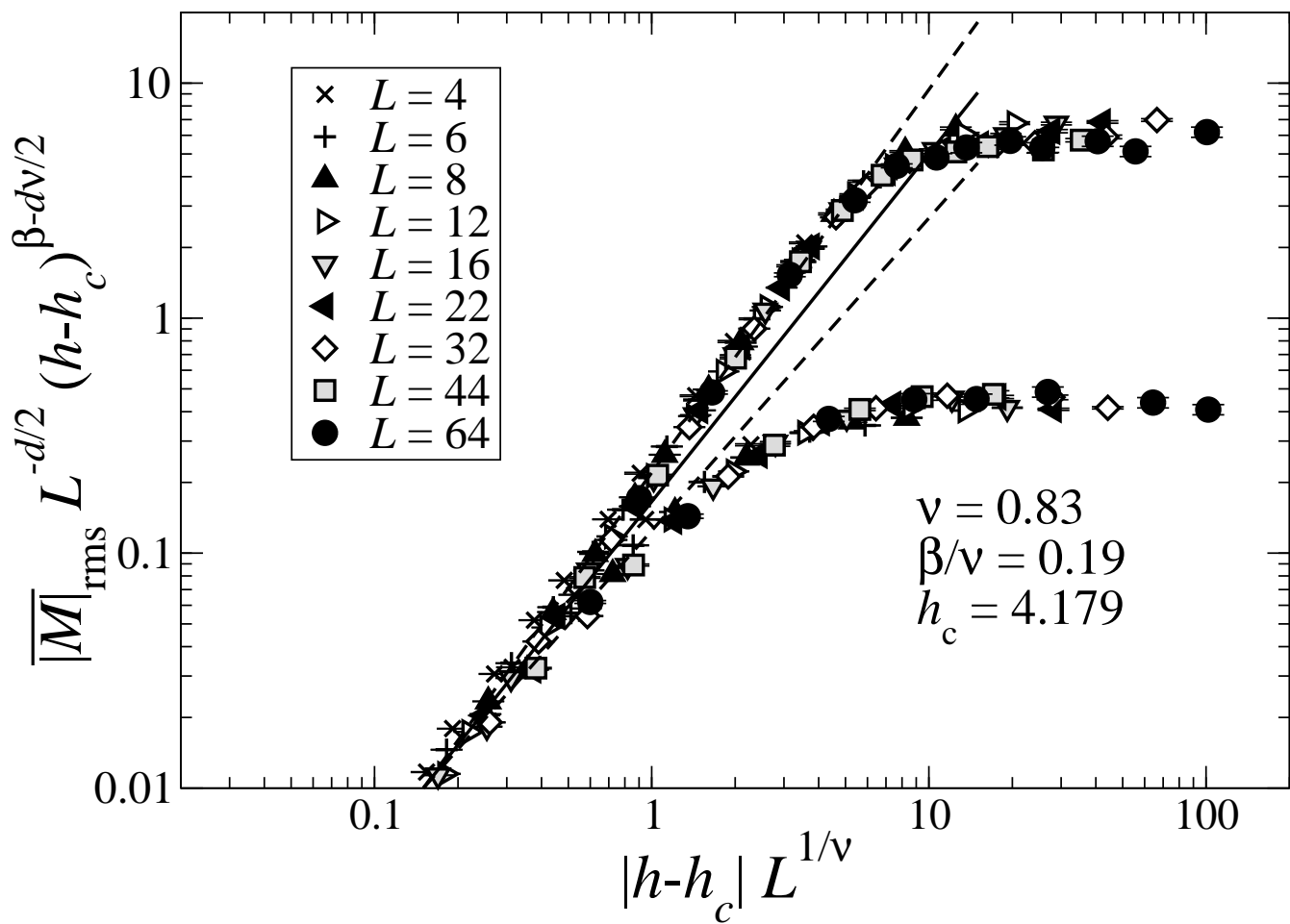


Figure 5

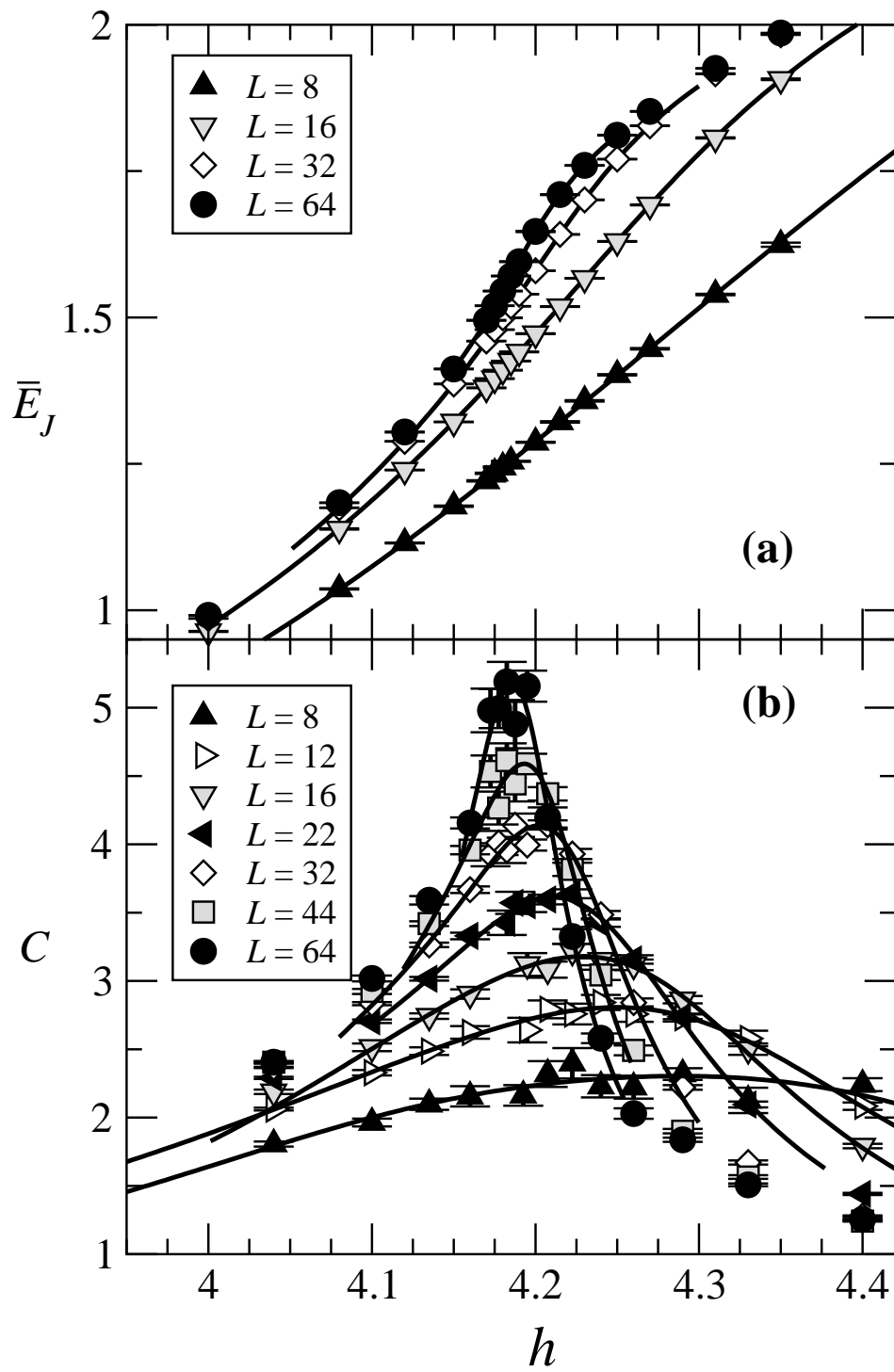


Figure 6

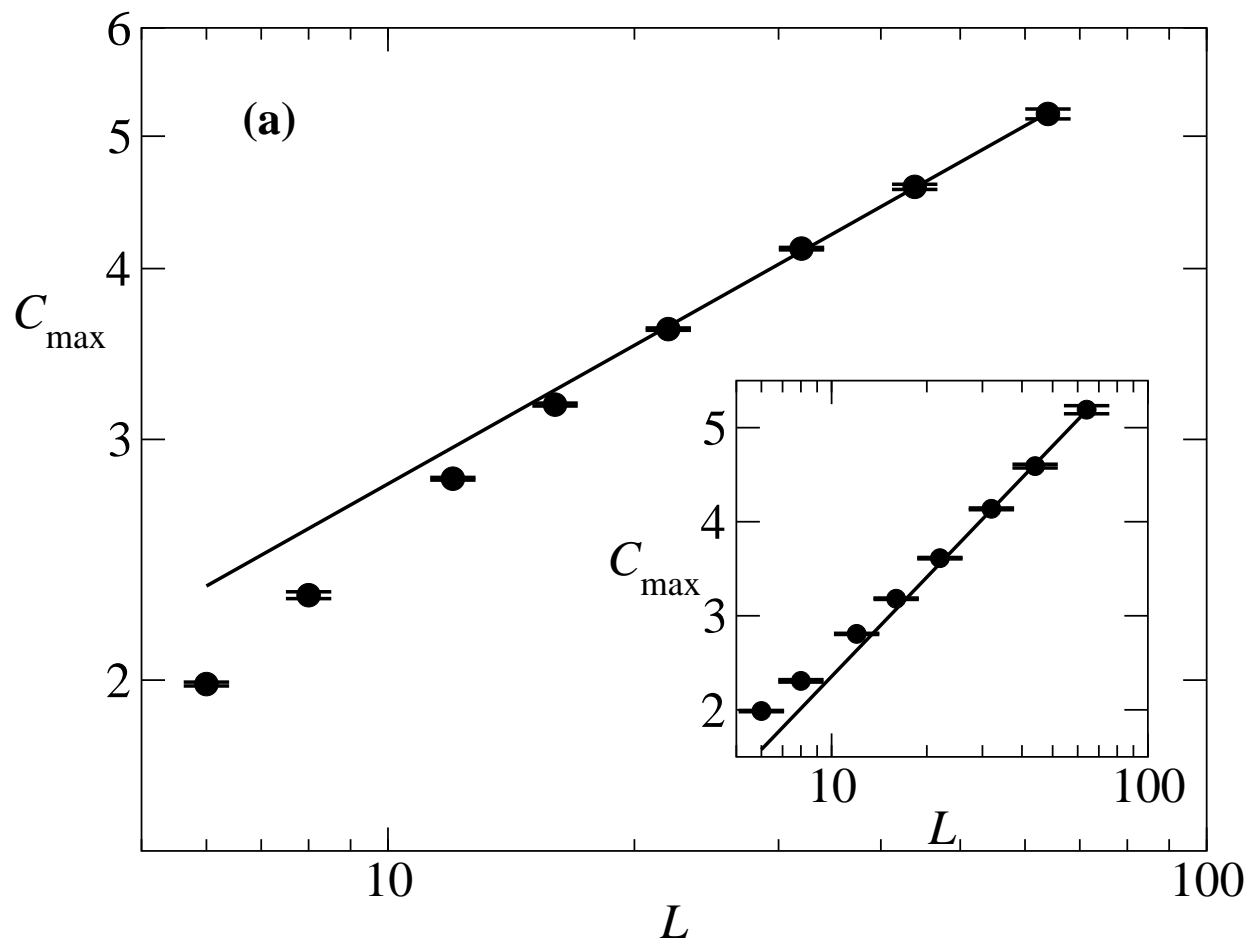


Figure 7a

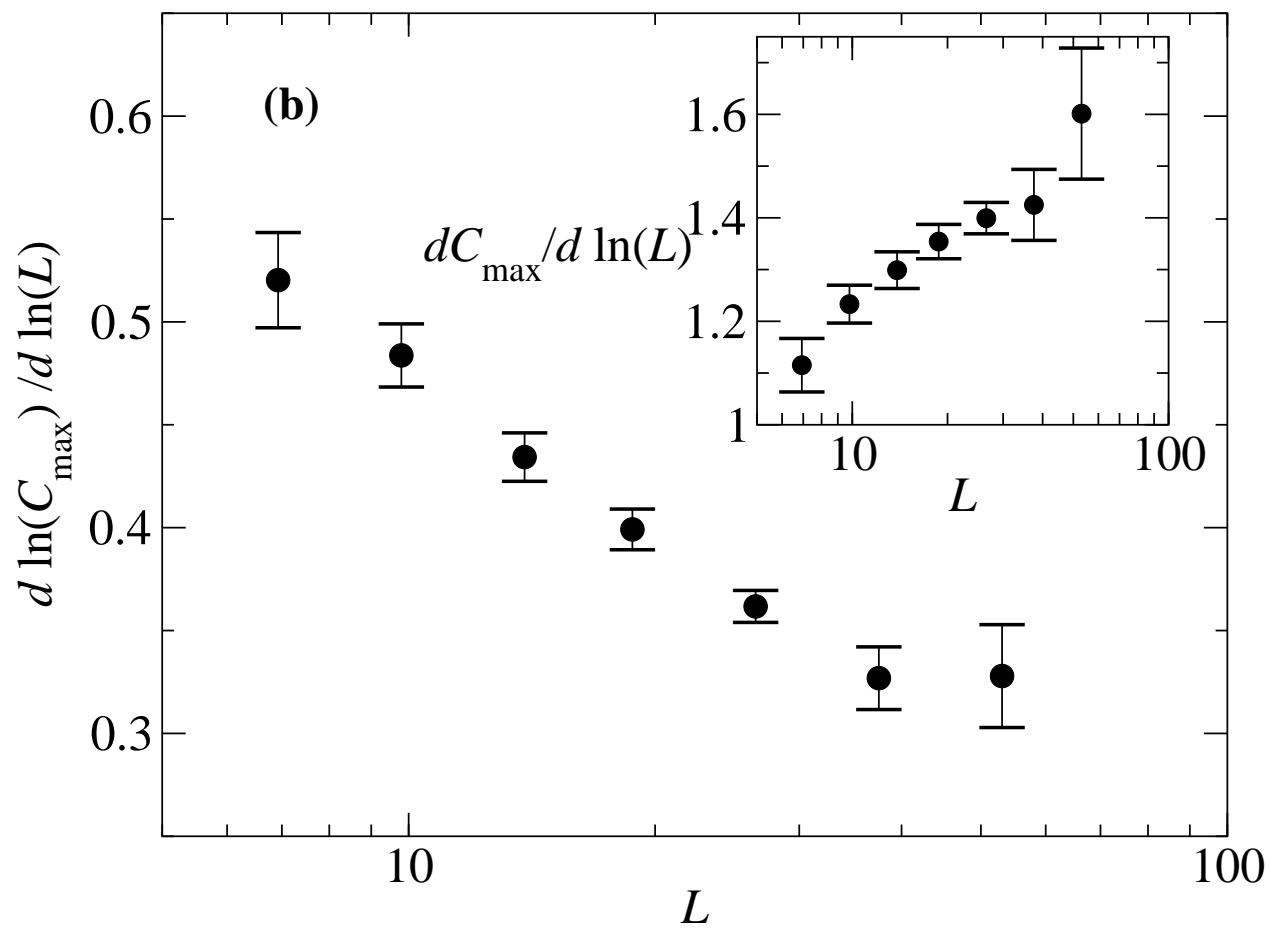


Figure 7b

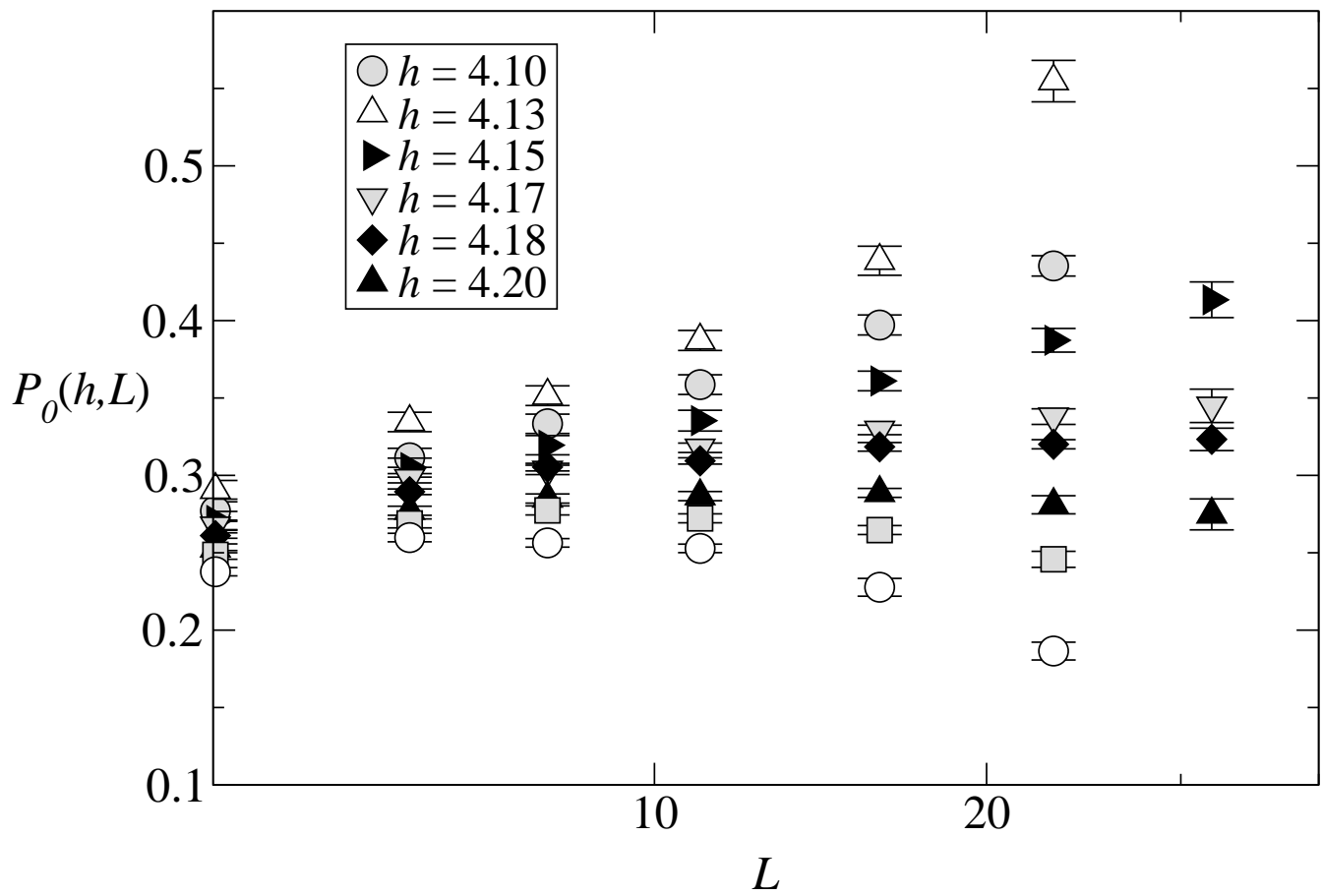


Figure 8

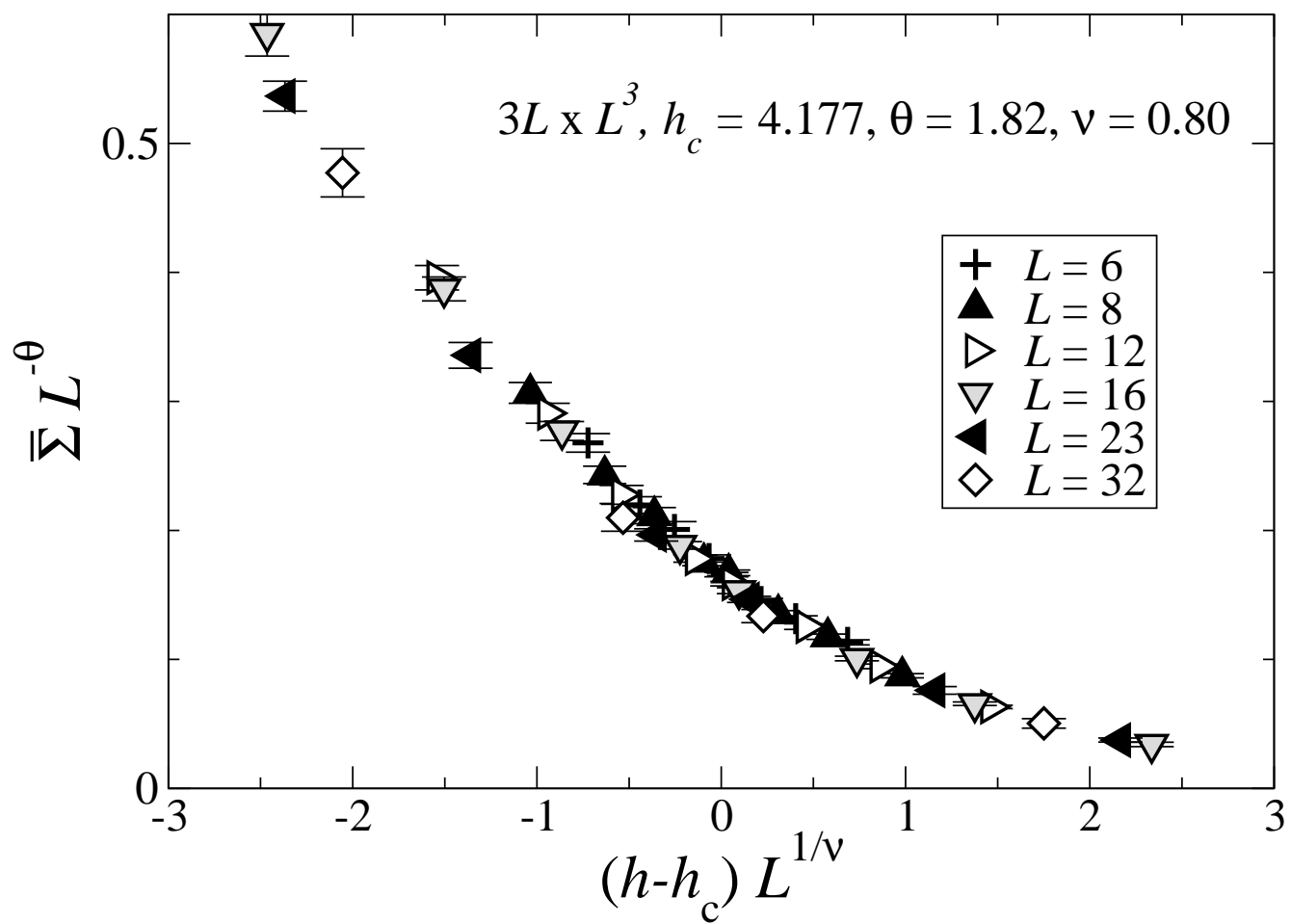


Figure 9

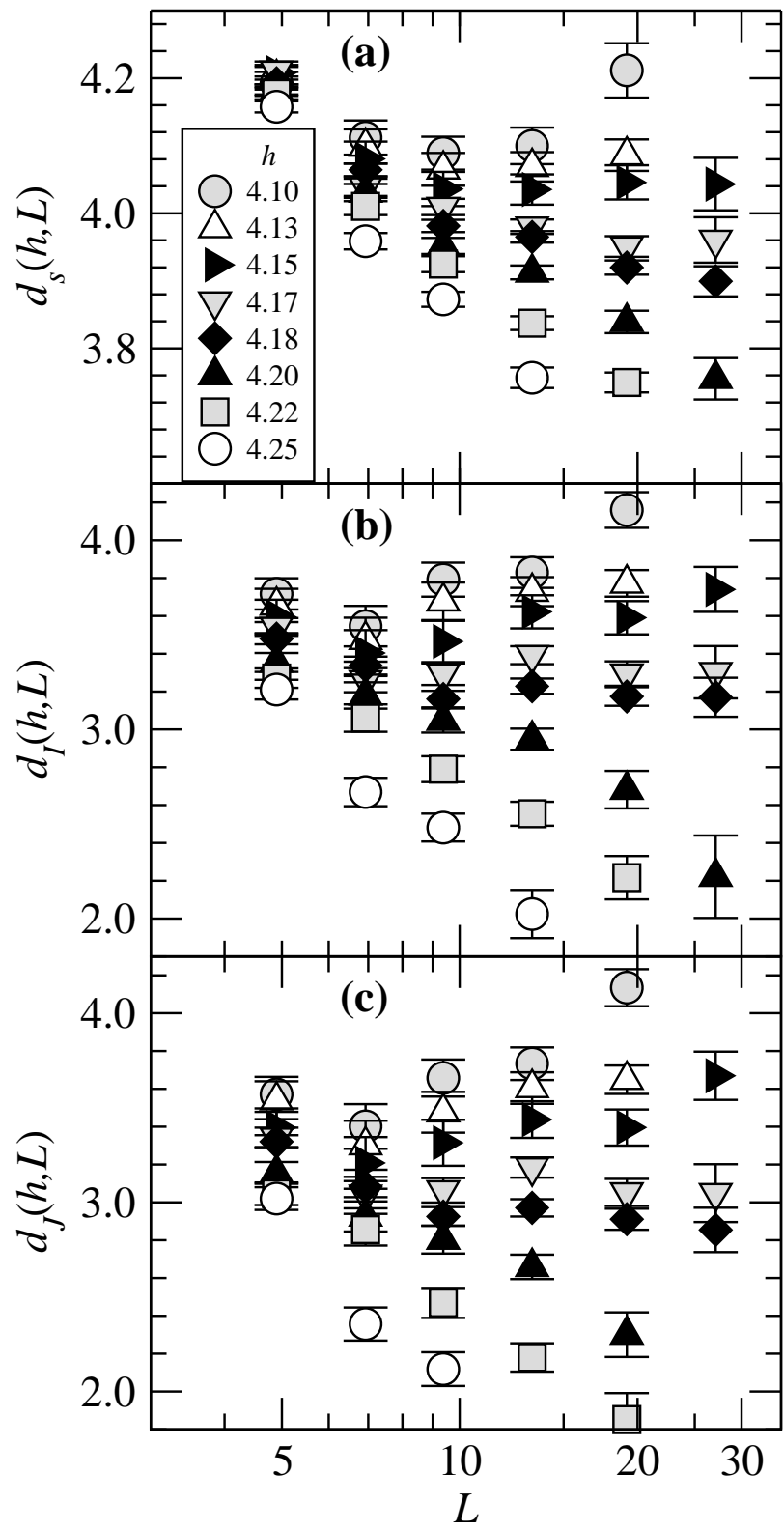


Figure 10

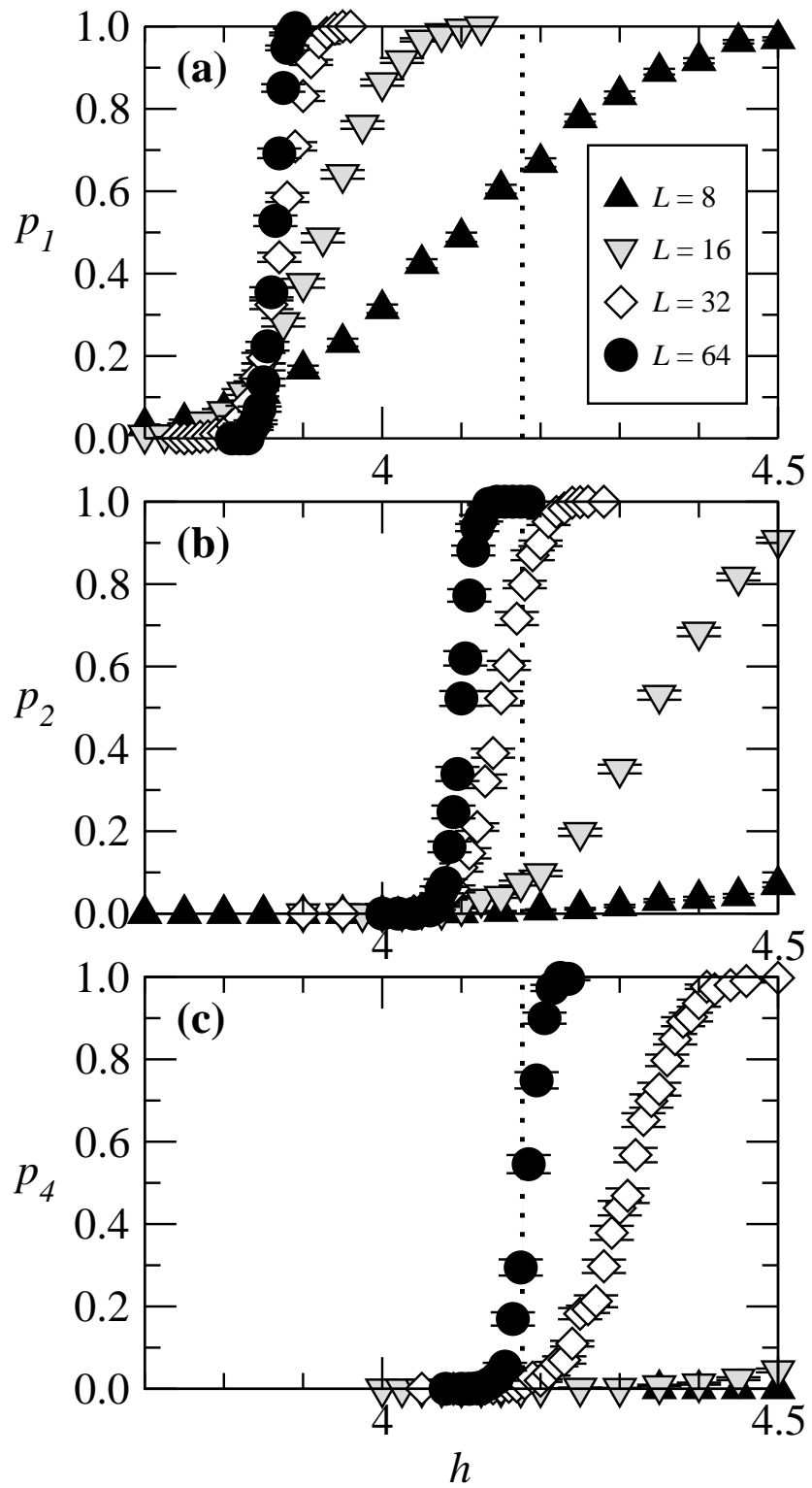


Figure 11

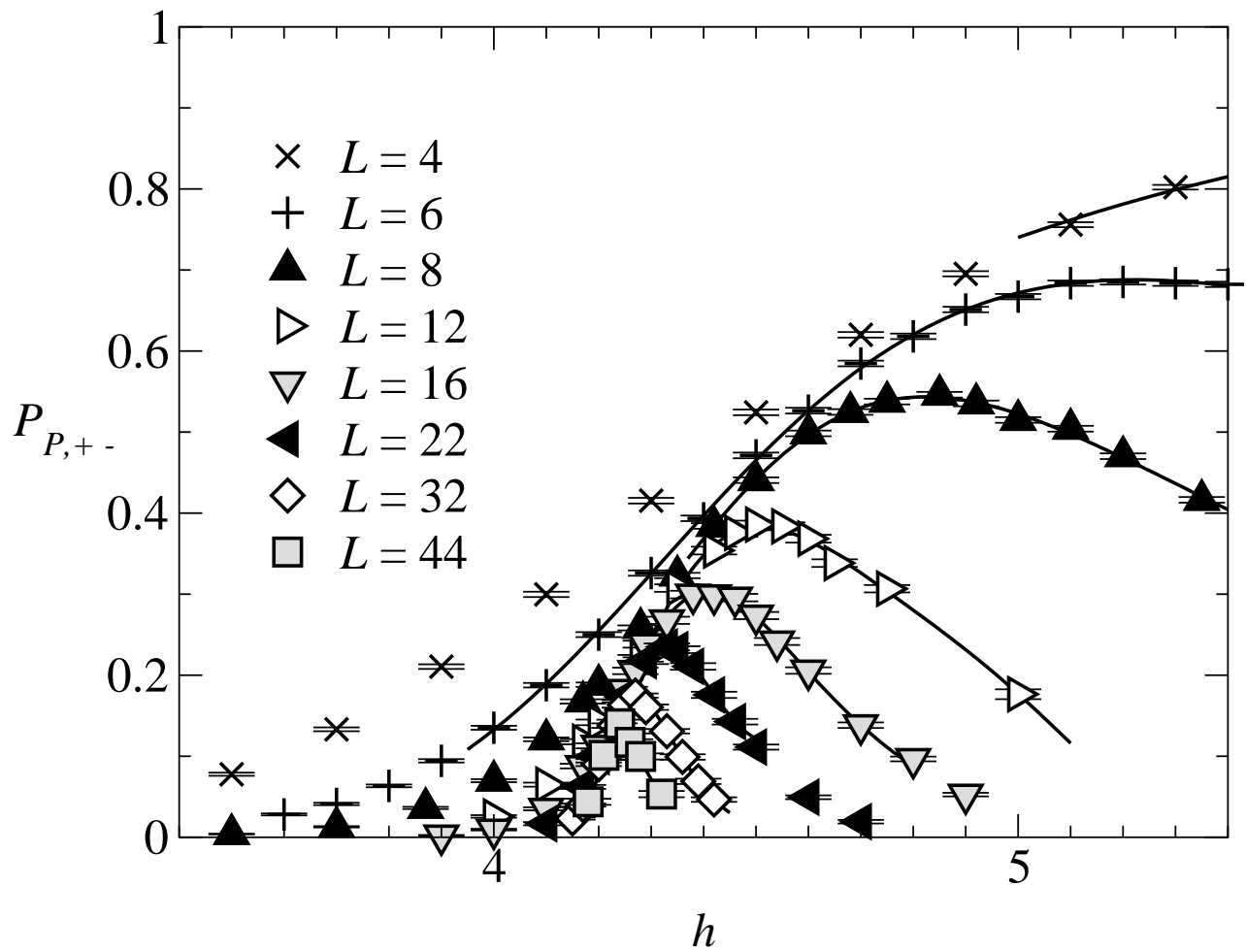


Figure 12

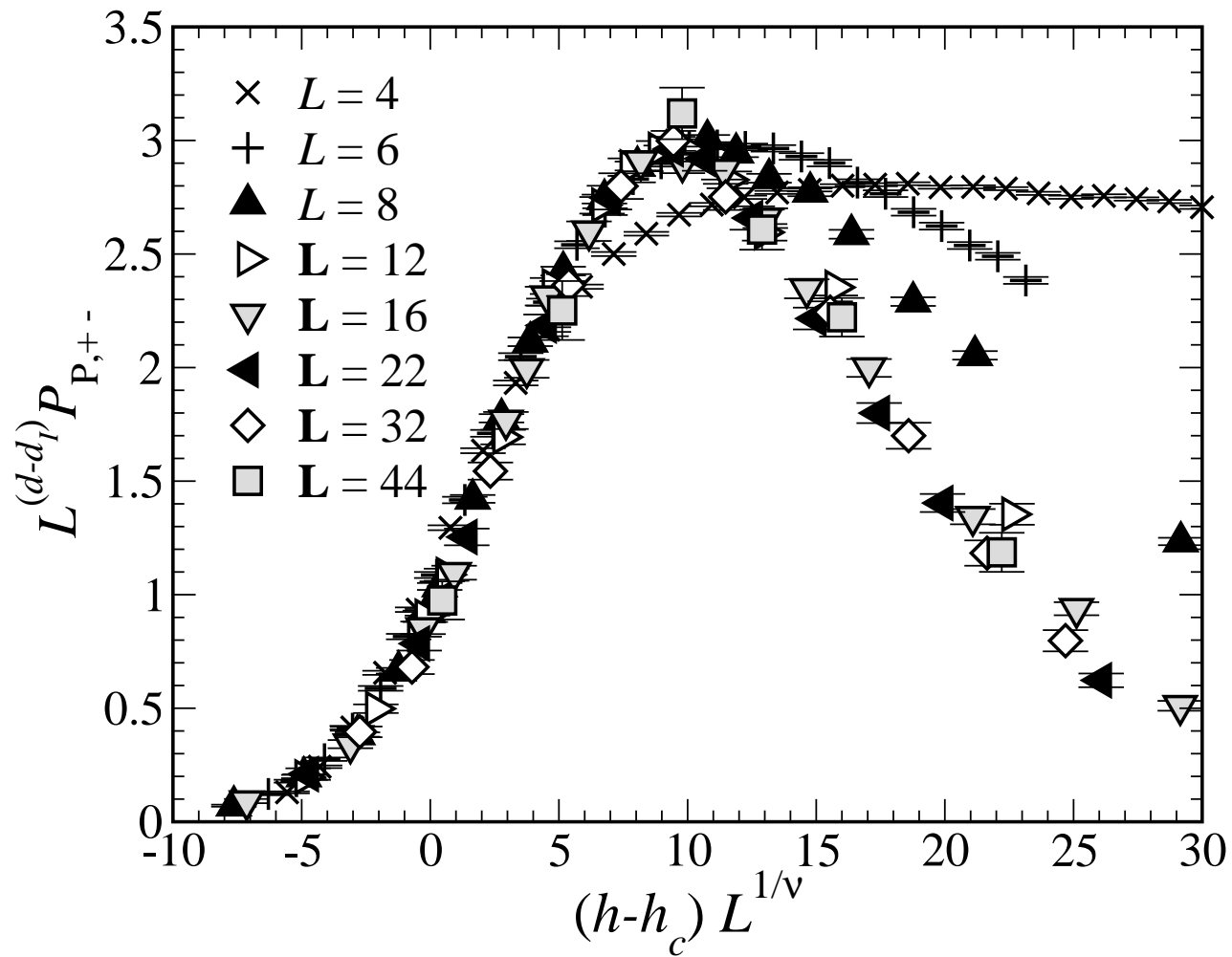


Figure 13

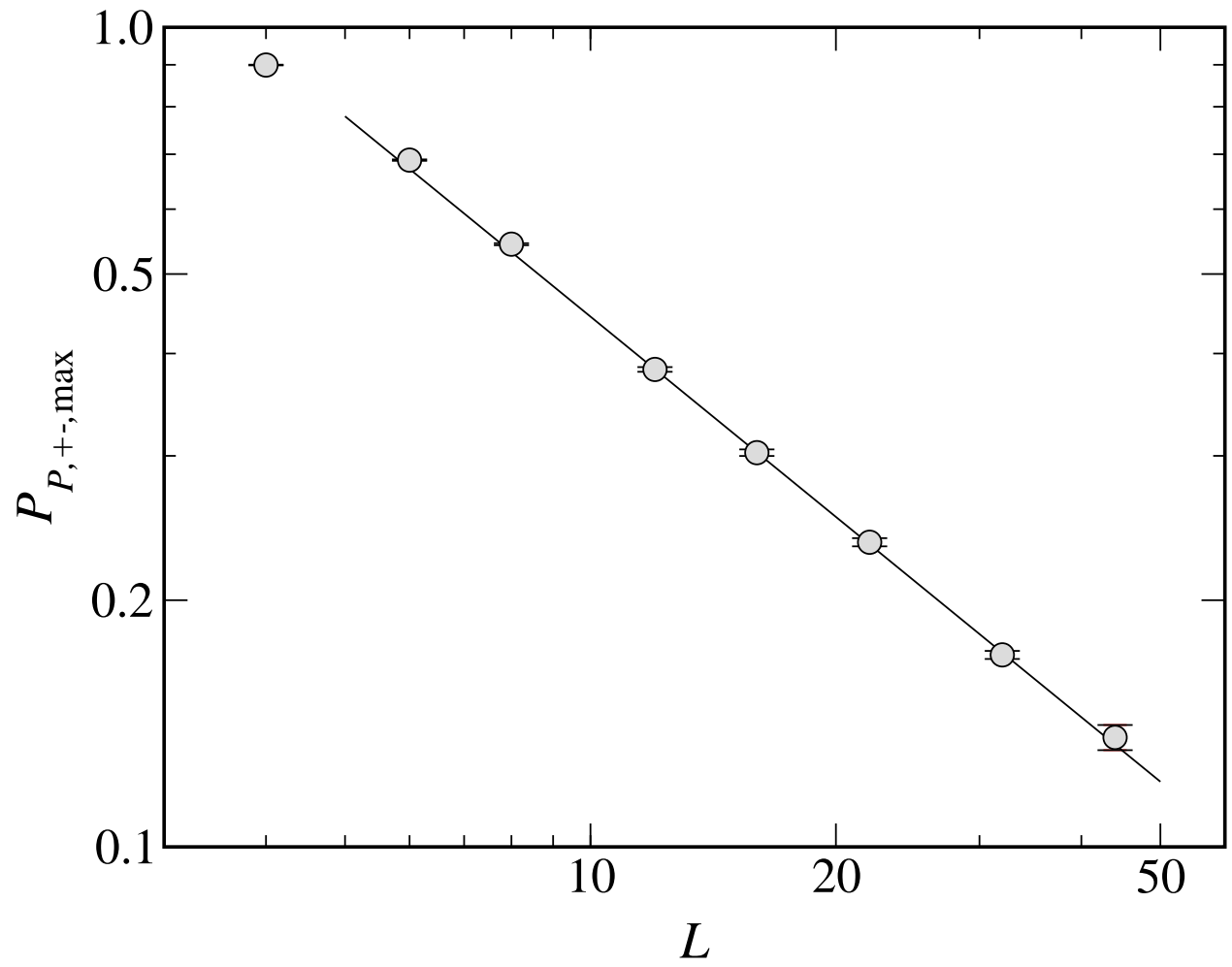


Figure 14

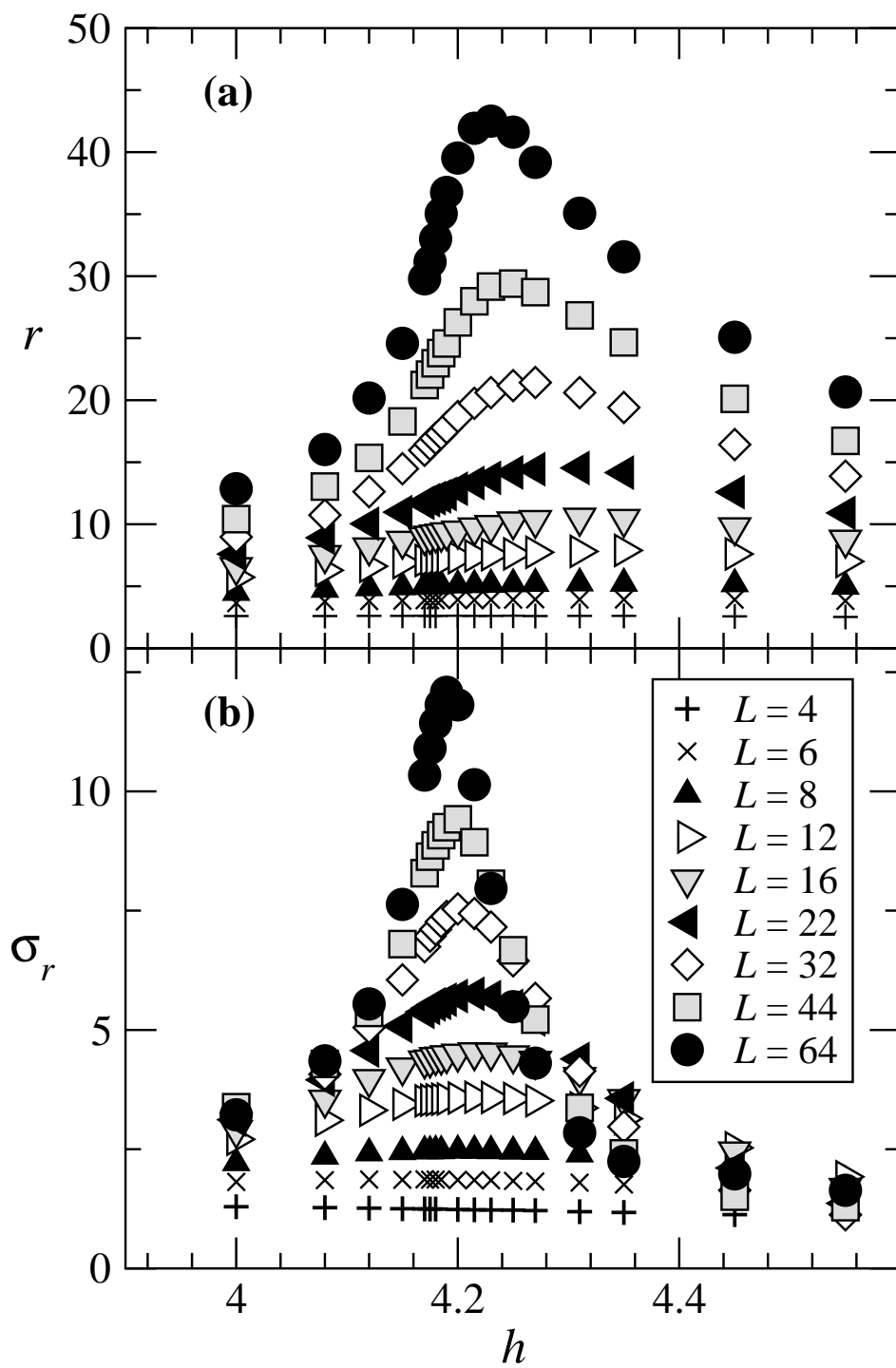


Figure 15

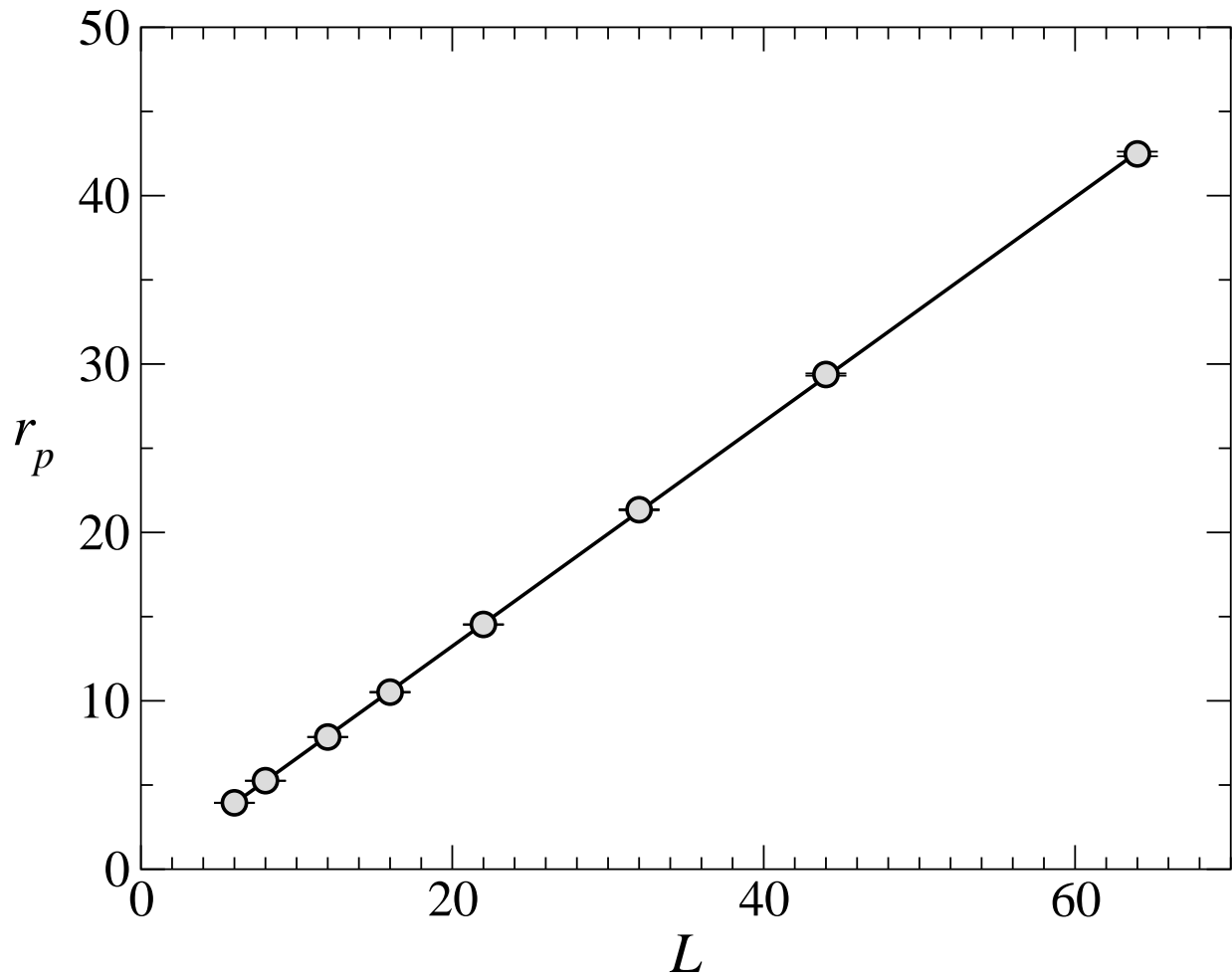


Figure 16